



**HAL**  
open science

## Quantifying the Uncertainty of a Coupled Plume and Tephra Dispersal Model: PLUME-MOM/HYSPLIT Simulations Applied to Andean Volcanoes

M. Alessandro Tadini, Olivier Roche, Pablo Samaniego, A. Guillin, N. Azzaoui, Mathieu Gouhier, M De'Michieli, F. Pardini, Julia Eychenne, B. Bernard, et al.

### ► To cite this version:

M. Alessandro Tadini, Olivier Roche, Pablo Samaniego, A. Guillin, N. Azzaoui, et al.. Quantifying the Uncertainty of a Coupled Plume and Tephra Dispersal Model: PLUME-MOM/HYSPLIT Simulations Applied to Andean Volcanoes. *Journal of Geophysical Research: Solid Earth*, 2020, 125 (2), 10.1029/2019JB018390 . hal-02453781v1

**HAL Id: hal-02453781**

**<https://uca.hal.science/hal-02453781v1>**

Submitted on 19 Nov 2020 (v1), last revised 17 Nov 2020 (v2)

**HAL** is a multi-disciplinary open access archive for the deposit and dissemination of scientific research documents, whether they are published or not. The documents may come from teaching and research institutions in France or abroad, or from public or private research centers.

L'archive ouverte pluridisciplinaire **HAL**, est destinée au dépôt et à la diffusion de documents scientifiques de niveau recherche, publiés ou non, émanant des établissements d'enseignement et de recherche français ou étrangers, des laboratoires publics ou privés.



Distributed under a Creative Commons Attribution 4.0 International License

# 1 **Quantifying the uncertainty of a coupled plume and tephra dispersal** 2 **model: PLUME-MOM/HYSPLIT simulations applied to Andean volcanoes**

3

4 A. Tadini<sup>1</sup>, O. Roche<sup>1</sup>, P. Samaniego<sup>1,2</sup>, A. Guillin<sup>3</sup>, N. Azzaoui<sup>3</sup>, M. Gouhier<sup>1</sup>, M. de' Michieli  
5 Vitturi<sup>4</sup>, F. Pardini<sup>4</sup>, J. Eychehenne<sup>1</sup>, B. Bernard<sup>2</sup>, S. Hidalgo<sup>2</sup>, J. L. Le Pennec<sup>1,5</sup>

6

7 <sup>1</sup>Laboratoire Magmas et Volcans, Université Clermont Auvergne, CNRS, IRD, OPGC, F-63000 Clermont-  
8 Ferrand, France.

9 <sup>2</sup>Escuela Politécnica Nacional, Instituto Geofísico, Ladrón de Guevara E11-253 y Andalucía, Quito, Ecuador

10 <sup>3</sup>Laboratoire de Mathématiques Blaise Pascal, Université Clermont Auvergne, CNRS, IRD, OPGC, F-63000  
11 Clermont-Ferrand, France.

12 <sup>4</sup>Istituto Nazionale di Geofisica e Vulcanologia, Sezione di Pisa, Via Cesare Battisti 53, 56126, Pisa, Italy

13 <sup>5</sup>Institut de Recherche pour le Développement, Alemania N32-188 y Guayanas, Quito, Ecuador

14

15 Corresponding author: Alessandro Tadini ([Alessandro.TADINI@uca.fr](mailto:Alessandro.TADINI@uca.fr))

16

## 17 **Keypoints**

- 18 • We present an uncertainty quantification for a coupled version of a plume model  
19 (PLUME-MoM) and a tephra dispersal model (HYSPLIT)
- 20 • The model has been tested against field data of 4 eruptions from Andean volcanoes (in  
21 Ecuador and Chile) of different magnitudes/styles
- 22 • The main conclusion of the uncertainty quantification is that the model is best suited  
23 for hazard studies of higher magnitude eruptions

24

25

26

27

28

29

30

31

32

33

## 34 **Abstract**

35 Numerical modelling of tephra dispersal and deposition is essential for evaluation of volcanic  
36 hazards. Many models consider reasonable physical approximations in order to reduce  
37 computational times, but this may introduce a certain degree of uncertainty in the simulation  
38 outputs. The important step of uncertainty quantification is dealt in this paper with respect to a  
39 coupled version of a plume model (PLUME-MoM) and a tephra dispersal model (HYSPLIT).  
40 The performances of this model are evaluated through simulations of four past eruptions of  
41 different magnitudes and styles from three Andean volcanoes, and the uncertainty is  
42 quantified by evaluating the differences between modeled and observed data of plume height  
43 (at different time steps above the vent) as well as mass loading and grain size at given  
44 stratigraphic sections. Different meteorological datasets were also tested and had a sensible  
45 influence on the model outputs. Other results highlight that the model tends to underestimate  
46 plume heights while overestimating mass loading values, especially for higher magnitude  
47 eruptions. Moreover, the advective part of HYSPLIT seems to work more efficiently than the  
48 diffusive part. Finally, though the coupled PLUME-MoM/HYSPLIT model generally is less  
49 efficient in reproducing deposit grain sizes, we propose it may be used for hazard maps  
50 production for higher magnitude eruptions (sub-Plinian or Plinian) for what concern mass  
51 loading.

52

## 53 **Index Terms and Keywords**

54 4314 Mathematical and computer modeling, 3275 Uncertainty quantification, 8428 Explosive  
55 volcanism, 8488 Volcanic hazards and risks

56 Tephra fall, tephra dispersal, numerical modelling, uncertainty quantification, Andean  
57 volcanoes

58

## 59 **1. Introduction**

60

61 Volcanic tephra dispersal and deposition represent a threat for many human activities  
62 since tephra may have a huge impact on aviation and can also damage edifices, infrastructures  
63 and vegetation when it accumulates on the ground, even in relatively small quantities. For this  
64 reason, numerical models have been developed over the past decades for describing both  
65 tephra rise into the eruptive column (plume models - PMs) or its transport by wind advection  
66 [tephra transport and dispersal models - TTDM; *Folch*, 2012]. Since describing in great detail  
67 the physics of such phenomena requires complex 3-D multiphase models, it is useful for  
68 operational purposes (e.g. volcanic ash tracking in real time or hazard maps production) to  
69 rely on simplified models, which introduce reasonable physical assumptions. In doing so,  
70 though computational times might be reduced, approximations and uncertainties are  
71 introduced in the final results of the simulations. Uncertainties need to be therefore quantified  
72 in order to facilitate decision makers in taking both real-time and long-term informed  
73 decisions. With respect to numerical models, uncertainty quantification in literature has been  
74 done: i) for PMs, by comparing modelled and observed values of maximum plume height (or  
75 level of neutral buoyancy) and/or of the mass flow rate (in kg/s), as for instance in *Folch et al.*  
76 [2016] or *Costa et al.* [2016]; ii) for TTDMs, by comparing modelled and observed ground  
77 deposit measurements (mass loadings in  $\text{kg/m}^2$ ) and/or ash cloud measurements

78 (concentrations in the atmosphere in  $\text{kg/m}^3$ ) [e.g., *Scollo et al.*, 2008; *Costa et al.*, 2009;  
79 *Bonasia et al.*, 2010; *Folch*, 2012].

80 The aim of the present study is therefore twofold. Firstly, we present a coupled version  
81 of two different models: i) a renewed version of PLUME-MoM, a simplified 1-D plume  
82 model developed by *de'Michieli Vitturi et al.* [2015], and ii) the HYSPLIT model [*Stein et al.*,  
83 2015], a Lagrangian TTDM developed by the National Oceanic and Atmospheric  
84 Administration (NOAA) and currently used by several Volcanic Ash Advisory Centers  
85 (VAACs) to track and forecast volcanic clouds. Secondly, we provide a quantification of the  
86 uncertainty of the coupled version of these two models by testing simulations results with data  
87 of four different recent eruptions of three Andean volcanoes (Fig. 1). These eruptions were  
88 produced by Cotopaxi [2015 eruption, *Bernard et al.*, 2016a] and Tungurahua [2006 eruption,  
89 *Eychenne et al.*, 2012; 2013 eruption, *Parra et al.*, 2016] volcanoes in Ecuador, and Puyehue-  
90 Cordón Caulle volcanic complex [2011 eruption, *Pistolesi et al.*, 2015] in Chile. With this  
91 new coupled model the volcanic particles transport is simulated throughout the whole process  
92 that is within the eruptive column and through atmospheric dispersion. Furthermore, the  
93 uncertainty quantification represents an important aspect regarding hazard maps production.

94 In this article, after describing the eruptions chosen for the uncertainty quantification  
95 (section 2.1), we present the PLUME-MoM and HYSPLIT models as well as the coupling of  
96 these two models (section 2.2.1). Then we present the input parameters used for the  
97 simulations (Section 2.2.2) and we describe the strategy adopted for the quantification of the  
98 uncertainty of the coupled model (Section 2.3). Results presented in Section 3 serve as a basis  
99 for the discussion in Section 4 about the uncertainties related to the input parameters and the  
100 numerical models and about also the effectiveness of these models when used for producing  
101 tephra fallout hazard maps.

## 102 103 **2. Background**

### 104 **2.1 Eruptions selected**

105 The four eruptions chosen for testing our simulations cover a wide range of eruptive  
106 styles (sub-Plinian, violent strombolian, vulcanian, hydrovolcanic to long-lasting ash  
107 emission), durations (from few hours up to more than 3 months) and magma compositions  
108 (andesitic to rhyolitic/rhyodacitic). The criteria for selecting these eruptions were i) the  
109 location of the volcanoes in the same geodynamic context, ii) the existence of both detailed  
110 chronologies and meteorological data for the eruptions, and iii) the availability of reasonably  
111 well constrained input parameters for the models.

#### 112 *2.1.1 Cotopaxi 2015*

113 The 2015 eruption of Cotopaxi (C15 – Fig. 1a) started with hydromagmatic explosions  
114 on August 14<sup>th</sup> 2015, which produced a 9-10 km-high eruptive column above the crater and  
115 moderate ash fallout to the NW of the volcano. Then, it was followed by three and a half  
116 months of moderate to low ash emissions with plumes reaching on average 2 km above the  
117 crater and directed mostly to the west [*Bernard et al.*, 2016a; *Gaunt et al.*, 2016].

118 The magmatic character of the eruption increased through time as was shown by  
119 microtextural analysis [*Gaunt et al.*, 2016] and ash/gas geochemistry [*Hidalgo et al.*, 2018].  
120 Through frequent sampling missions, the ash emission rate was calculated and correlated with  
121 the eruptive tremors, and it decreased during three emission phases following the conduit  
122 opening [*Bernard et al.*, 2016a].

123 The fallout deposit was characterized by a very fine-grained ash with mostly blocky  
124 fragments and few vesicular scoria [*Gaunt et al.*, 2016]. The hydrothermal components were  
125 dominant at the onset of the eruption but rapidly faded and were replaced by juvenile material

126 [Gaunt *et al.*, 2016]. In total, this eruption emitted  $\sim 1.2 \times 10^9$  kg of ash and was characterized  
 127 as a VEI 1-2 [Bernard *et al.*, 2016a].

### 128 2.1.2 Tungurahua 2013

129 According to Hidalgo *et al.* [2015], the eruptive phase XI (T13) at Tungurahua  
 130 volcano (Fig. 1a) started on July 14<sup>th</sup> 2013 and lasted 23 days. A vulcanian onset, interpreted  
 131 as the opening of a plugged conduit, was followed by a paroxysm which created a  $\sim 14$  km-  
 132 high eruptive column [Parra *et al.*, 2016]. The ash cloud created during this eruption was  
 133 divided into a high cloud ( $\sim 8$ -9 km above the crater) moving north and an intermediate cloud  
 134 ( $\sim 5$  km above the crater) moving west and that produced most of the ash fallout [Parra *et al.*,  
 135 2016]. The eruption intensity dropped after this paroxysm but ash emission continued with a  
 136 secondary increase between July 20<sup>th</sup> and 24<sup>th</sup>. Finally the eruption stopped at the beginning  
 137 of August.

138 In total, this eruption emitted  $\sim 6.7 \times 10^8$  kg of fallout deposits ( $\sim 2.9 \times 10^8$  kg for the first  
 139 day) and  $\sim 5 \times 10^9$  kg of pyroclastic flow deposits (mostly during the first day) [García Moreno,  
 140 2016; Parra *et al.*, 2016].

141 Parra *et al.* [2016] performed numerical simulations of the vulcanian onset of this  
 142 eruption, which occurred on July 14<sup>th</sup> 2013, using the coupled WRF-FALL3D models  
 143 [Michalakes *et al.*, 2001; Folch *et al.*, 2009]. By comparing the mass loading between the  
 144 modeled values and the observed ones at four sampling sites, the above-mentioned authors  
 145 derived a set of Eruptive Source Parameters (ESPs) useful for operational purposes in case of  
 146 vulcanian eruptions at Tungurahua volcano.

### 147 2.1.3 Tungurahua 2006

148 At Tungurahua volcano (Fig. 1a), a paroxysmal eruption (T06) occurred on August  
 149 16<sup>th</sup> 2006, which was accompanied by regional tephra fallout and many scoria flows and  
 150 surges that devastated the western half of the edifice [Douillet *et al.*, 2013; Hall *et al.*, 2013].  
 151 This eruption was characterized by vigorous lava jetting and fountaining, a vent-derived  
 152 eruption column reaching 16–18 km above the vent [Steffke *et al.*, 2010; Eychenne *et al.*,  
 153 2012], numerous Pyroclastic Density Currents (PDCs) descending the southern, western and  
 154 northern flanks of the volcano [Kelfoun *et al.*, 2009; Bernard *et al.*, 2014], and a massive  
 155 blocky lava flow emplacing on the western flank while the explosive activity waned  
 156 [Samaniego *et al.*, 2011; Bernard *et al.*, 2016b]. At the climax of the eruptive event, after 3  
 157 hours of intense PDC formation, the vent-derived ash plume developed into a sub-vertical and  
 158 sustained column for 50 to 60 minutes [Hall *et al.*, 2013]. The plume spread over the Inter-  
 159 Andean Valley, west of the volcano, and reached the Pacific Ocean, leading to substantial  
 160 lapilli and ash fallout on the nearby communities and cities (e.g., Riobamba and Ambato)  
 161 located to the West. The intense PDC activity generated ash-rich, 10 km-high co-PDC plumes  
 162 that spread over the same areas and deposited fine ash ( $< 90 \mu\text{m}$ ) [Eychenne *et al.*, 2012;  
 163 Bernard *et al.*, 2016b].

164 In total, the whole August 2006 eruption produced  $39.3 \pm 5.1 \times 10^6 \text{ m}^3$  of fallout deposit  
 165 (both vent-derived and co-PDC derived) of which  $24.9 \pm 3.3 \times 10^9$  kg were related to the vent-  
 166 derived fall [Bernard *et al.*, 2016b].  
 167

### 168 2.1.4 Puyehue-Cordón Caulle 2011

169 According to Collini *et al.* [2013], the Puyehue-Cordón Caulle 2011 eruption (PCC11  
 170 - Fig. 1b) started on June 4<sup>th</sup> at 14:45 LT (18:45 UTC) with the opening of a new vent 7 km

171 NNW from the main crater of the Puyehue-Cordón Caulle complex (“We Pillán” vent – Fig.  
 172 1b). The eruptive period, which involved mainly magma of rhyolitic-rhyodacitic composition  
 173 [Bonadonna *et al.*, 2015a], lasted up to June 2012 [Jay *et al.*, 2014] and comprised both  
 174 explosive and effusive activity [Tuffen *et al.*, 2013]. The main explosive phase, which  
 175 dispersed most of the tephra toward E and SE, lasted approximately 17-27 hours [Jay *et al.*,  
 176 2014; Bonadonna *et al.*, 2015b]. During the first three days of the eruption, the column rose  
 177 approximately between 9 and 12 km above vent, then between 4 and 9 km during the  
 178 following week, and less than 6 km after June 14<sup>th</sup> [Bonadonna *et al.*, 2015a; Biondi *et al.*,  
 179 2017].

180 During the eruption, the mass eruption rate (MER) fluctuated between  $2.8 \times 10^7$  (during  
 181 the first days) and less than  $5 \times 10^5$  kg/s after June 7<sup>th</sup> [Bonadonna *et al.*, 2015b]. Pistolesi *et*  
 182 *al.* [2015] subdivided the stratigraphic record in thirteen tephra layers: among them, the first  
 183 unit (Unit I, layers A-F) represented the tephra deposited between June 4<sup>th</sup>-5<sup>th</sup>. Unit I had a  
 184 total erupted mass of  $4.5 \pm 1.0 \times 10^{11}$  kg and was sub-Plinian with a VEI of 4 [Bonadonna *et al.*,  
 185 2015b]. Bonadonna *et al.* [2015a] calculated the total grain size distribution (TGSD) of Unit I  
 186 in the range  $-4\phi/11\phi$ , using different datasets and methods. The results indicated a bimodal  
 187 distribution with the two sub-populations (with modes at  $-2\phi$  and  $7\phi$ ) separated by the  $3\phi$   
 188 grain size [Bonadonna *et al.*, 2015a].

189 Collini *et al.* [2013] performed numerical modellings of this eruption between June 4<sup>th</sup>  
 190 to June 20<sup>th</sup> using the above-mentioned WRF-FALL3D code. The authors compared both the  
 191 column mass load (in ton/km<sup>2</sup>) and ground deposit measurements between modeled and  
 192 observed values. With respect to deposit thickness measurements, they compared deposit  
 193 thicknesses at 37 locations, resulting in a best-fit line on a computed versus observed graphs.  
 194 The PCC11 eruption was furthermore modeled by Marti *et al.* [2017], who simulated the  
 195 eruption from June 4<sup>th</sup> up to Jun 21<sup>st</sup> using the NMMB-MONARCH-ASH model and  
 196 compared the same parameters as in Collini *et al.* [2013]. For the ground measurements, they  
 197 provided comparisons between the simulated and observed isopach maps for both the Unit I  
 198 and other eruptive units cited in Pistolesi *et al.* [2015], finding a good agreement between  
 199 modeled and observed data.

## 200 2.2 Numerical modeling

### 201 2.2.1 Models used and coupling of the codes

202 For this work, the integral plume model PLUME-MoM has been coupled with  
 203 HYSPLIT, one of the most extensively used atmospheric transport and dispersion models in  
 204 the atmospheric sciences community.

205 Following the approach adopted in Bursik [2001], PLUME-MoM solves the equations  
 206 for the conservation of mass, momentum, energy, and the variation of heat capacity and  
 207 mixture gas constant. The model accounts for particle loss during the plume rise and for radial  
 208 and crosswind air entrainment parameterized using two entrainment coefficients. In contrast  
 209 to previous works, in which the pyroclasts are partitioned into a finite number of bins in the  
 210 Krumbein scale, PLUME-MoM adopts the method of moments to describe a continuous size  
 211 distribution of one or more group of particles (i.e. juveniles, lithics...). An uncertainty  
 212 quantification and a sensitivity analysis of the PLUME-MoM model were done by  
 213 de'Michieli Vitturi *et al.* [2016] by analyzing the distribution of plume heights obtained when  
 214 varying a series of input parameters (i.e. air radial/wind entrainment, exit velocity, exit  
 215 temperature, water fraction and wind intensity). The above-mentioned authors showed that  
 216 plume height distribution was the widest when the parameters varied were the exit velocity,  
 217 exit temperature, water fraction and wind intensity. With respect to the sensitivity, de'Michieli  
 218 Vitturi *et al.* [2016] showed that initial water fraction had the strongest influence on plume

219 height determination (i.e. the plume height decreased by a factor of ~1.54 when increasing  
220 water content from 1 to 5 wt%).

221 HYSPLIT belongs to the family of Lagrangian Volcanic ash transport and dispersion  
222 models, which have been used operationally since the mid 1990's by the International Civil  
223 Aviation Organization (ICAO) to provide ash forecast guidance. The model solves the  
224 Lagrangian equations of motion for the horizontal transport of pollutants (i.e. particles), while  
225 vertical motion depends on the pollutant terminal fall velocity. The dispersion of a pollutant  
226 may be described using three main types of configuration, “3D particle” “puff” or hybrid  
227 “particle/puff”. Particularly, in the “puff” configuration, pollutants are described by packets of  
228 ash particles (“puffs”) having a horizontal Gaussian distribution of mass described by a  
229 standard deviation  $\sigma$ . The puffs expand with atmospheric turbulence until they exceed the size  
230 of the meteorological grid cell (either horizontally or vertically) and then split into several  
231 new puffs, each with their respective pollutant mass. In this work, the hybrid “particle/puff”  
232 configuration has been used, in which the horizontal packets of particles have a “puff”  
233 distribution, while in the vertical they move like 3D particles. This approach allows to use a  
234 limited number of puffs to properly capture both the horizontal dispersion and the vertical  
235 wind shears. *Webley et al.* [2009] have evaluated the sensitivity of the model with respect to  
236 the concentration of ash in the volcanic cloud when two parameters, TGSD and the vertical  
237 distribution of ash, were varied. The sensitivity analysis was done with respect to a test case  
238 eruption (Crater Peak/Mt. Spurr, Alaska, USA, 1992). They showed that three different  
239 TGSDs had little effect on the modeled ash cloud, while a uniform concentration of ash  
240 throughout the vertical eruptive column provided results more similar to satellite  
241 measurements. For this work, some modifications have been implemented in HYSPLIT and  
242 are described in Text S1 from the Supporting Information.

243 In the present study we coupled the PLUME-MoM and HYSPLIT models with an ad-  
244 hoc Python script, which computes for each grain size, from the output of the plume model,  
245 the mass rates released from the edges of the plume at intervals of fixed height, and the mass  
246 flow that reaches the neutral buoyancy level. Then, the script assembles an input file where  
247 the source locations for HYSPLIT are defined. In addition, it is employed a utility from the  
248 HYSPLIT package to extract the wind profile at the vent, in order to provide this information  
249 to the plume model. This coupled model was used for all the studied eruptions, while for  
250 some specific cases (i.e. the simulations for the PCC11 eruption) we also implemented a best-  
251 fitting inverse version of this coupling, which was based on the approach first described by  
252 *Connor and Connor* [2006] and applied, among others, by *Bonasia et al.* [2010] and *Costa et*  
253 *al.* [2009]. The parameters for which the inversion was performed and their range of variation  
254 were identified first. We considered the mass flow rate (in kg/s), the initial water mass  
255 fraction (in wt%) and the particle shape factor [*Wilson and Huang, 1979; Riley et al., 2003*].  
256 We chose these parameters because their uncertainty was higher and/or the models were more  
257 sensitive to small variations of them. The procedure was aimed at minimizing the  $T^2$  function

$$T^2 = \sum_{i=1}^N w_i [ML_{o,i} - ML_{m,i}]^2$$

258 where the sum is extended over  $N$  stratigraphic sections used in the inversion,  $w_i$  are  
259 weighting factors (in our case all are equal to 1),  $ML_{o,i}$  denotes the observed mass load (in  
260  $\text{kg/m}^2$ ) and  $ML_{m,i}$  are the values predicted by the model (in  $\text{kg/m}^2$ ). The values of  $T^2$  will be  
261 then compared to the standard Chi-2 distribution of  $N-p$  degrees of freedom, with  $p=3$  the  
262 number of free parameters.

263

264 *2.2.2 Modelling features and input parameters*

265 We tested four different types of meteorological data (GDAS, NCEP/NCAR, ERA-  
 266 Interim, ERA-Interim refined using WRF/ARW; see Text S1 from the Supporting  
 267 Information for details) with various spatial and temporal resolutions (see Table S1 in  
 268 Supporting Information), which correspond to the most widely used meteo data for studies  
 269 similar to ours.

270 All the HYSPLIT simulations were done using a  $0.05^\circ$  (~5 km) computational grid.  
 271 After the end of each emission time (i.e. the actual duration of the eruption), a further amount  
 272 of 12 hours was added to the simulation in order to allow finer particles to settle down.  
 273 Simulations were performed in a forward way for all the four eruptions. However, a best-  
 274 fitting inverse procedure (see Section 2.2.1) was performed for the PCC11 eruption because  
 275 the uncertainty in the tephra fallout total mass estimation was the highest among the four  
 276 chosen eruptions. A total of 600 inversions were performed, corresponding to 200 inversions  
 277 for each of the three meteo data employed for a given eruption (GDAS, NCEP/NCAR and  
 278 ERA-Interim).

279 Eruption source parameters (ESPs) were estimated from earlier works for the four  
 280 eruptions and some of them are reported in Table 1 (the detailed list of parameters for each  
 281 eruption is available in Table S2 in Supporting information). More specifically: a) the  
 282 computational grid dimension (i.e. the total span of the computational domain in degrees with  
 283 respect to the vent location) was defined in order to contain all or the vast majority (>95%) of  
 284 the erupted mass and to reduce as much as possible the computational time; b) the initial  
 285 water content was assumed as that of typical mean values for andesitic (for C15, T13 and  
 286 T06) or rhyolitic (for PCC11) magmas, following *Andújar et al.* [2017] and *Martel et al.*  
 287 [2018] respectively. For the inverse simulations of PCC11, the initial water content at each  
 288 iteration was sampled between 6% and 8% [*Martel et al.*, 2018]; c) Particles exit velocities  
 289 from the vent were assigned two different values [following *de'Michieli Vitturi et al.*, 2015]  
 290 corresponding to a “weak plume” case (C15 and T13) or to a “strong plume” case (T06 and  
 291 PCC11); d) The heat capacity of volcanic particles was assumed with a fixed value of 1600  
 292 J/kgxK following *Folch et al.* [2016]; e) The particles shape factor was assumed with two  
 293 different values for andesitic magmas (C15, T13 and T06) and for rhyolitic ones (PCC11)  
 294 following the results of *Riley et al.* [2003]. For the inverse simulations of the PCC11 eruption,  
 295 the particle shape factor values at each iteration were sampled between 0.6 and 0.8 [*Riley et*  
 296 *al.*, 2003]; h) the particle density values were assumed to vary linearly between two values ( $\rho_1$   
 297 and  $\rho_2$ ) specific of two grain sizes ( $\phi_1$  and  $\phi_2$ ) according to *Bonadonna and Phillips* [2003].  
 298 Values of  $\rho_1$ ,  $\rho_2$ ,  $\phi_1$ , and  $\phi_2$  were taken from *Eychenne and Le Pennec* [2012] (C15/T13/T06)  
 299 and *Pistolesi et al.* [2015] (PCC11). For each eruption, all the other most relevant features of  
 300 input parameters are described below.

301 For the Cotopaxi C15 eruption, the simulations covered the whole eruption duration  
 302 (14/08/2015 - 30/11/2015) for a total of 108 days and 17 hours. Plume heights values were  
 303 obtained from *Bernard et al.* [2016a]. With respect to the TGSD calculated in *Gaunt et al.*  
 304 [2016] we also used several unpublished data (see Table S1 from the Supporting  
 305 Information). More specifically, a total of 33 samples representative of different times during  
 306 the eruption and from 4 stratigraphic sections were employed. The TGSD was derived from a  
 307 weighted mean (with respect to different mass loading values) of single grain size  
 308 measurements. MER values used for the simulations were recalculated from *Bernard et al.*  
 309 [2016a] to obtain hourly values (see Table S2 from the Supporting Information).

310 For the Tungurahua T13 eruption, the simulations also covered the whole eruption  
 311 duration (14/07/2013 – 30/07/2013) for a total of 16 days and 12 hours. We considered  
 312 observed plume height measurements from two sources: the ones by the Washington VAAC  
 313 using satellite measurements, and those from observations made by the Tungurahua Volcano

314 Observatory (OVT). Similarly to the C15 eruption, the TGSD was obtained from a weighted  
315 mean (with respect to different mass loading values) of single grain size measurements.  
316 Hourly values of MER were obtained from unpublished data of the total mass deposited at the  
317 Choglontus sampling site at different intervals (Table S2 from the Supporting Information).

318 For the Tungurahua T06 eruption, the simulations covered 4 hours corresponding to  
319 the climatic phases I and II described in *Hall et al.* [2013]. Plume heights were derived from  
320 *Steffke et al.* [2010]. An average value of the MER was initially derived from the total mass  
321 deposited over this period (see Text S1 from the Supporting Information); successively,  
322 hourly values of MER were determined after an iterative procedure aimed at obtaining  
323 modeled output values of plume heights as close as possible to observed data. This iteration  
324 was done separately for each meteo data. The TGSD was recalculated from that of *Eychenne*  
325 *et al.* [2012] by removing the mass contribution of the co-PDC part (see Text S1 from the  
326 Supporting Information).

327 Finally, for the Puyehue-Cordón Caulle PCC11 eruption, the simulations covered the  
328 initial part of the eruption corresponding to the emplacement of Unit I [*Pistolesi et al.*, 2015]  
329 for a total of 24 hours. Daily average plume heights and MERs from *Bonadonna et al.*  
330 [2015b] were employed along with a TGSD calculation from *Bonadonna et al.* [2015a]. For  
331 the inverse simulations, the MER was sampled between two values ( $10^{6.75}$  and  $10^{6.95}$  kg/s),  
332 which gave the minimum and maximum total mass values provided by *Bonadonna et al.*  
333 [2015b] and reported also in Table S2 (Supporting Information).

334

### 335 **2.3 Uncertainty quantification procedure**

336 We quantified the uncertainty of the coupled numerical model by comparing modeled  
337 and observed values of key parameters of both the PM and the TTDM.

338 With respect to the PM, we compared the plume height (in meters above vent)  
339 observed against the corresponding value at the same time (or at the closest measurement  
340 available) given by the model. In this case it is important to remember that plume height in  
341 PLUME-MoM is obtained as output value using a fixed MER.

342 For the TTDM, we compared ground deposit measurements and we adopted a specific  
343 approach in order to properly address uncertainty quantification. The results of the  
344 simulations were used to compare, at each stratigraphic section, observed and modeled values  
345 of mass loading and grain size, the latter one characterized by  $Md\phi$  and  $\sigma\phi$  [*Folk and Ward*,  
346 1957]. For mass loading we use hereafter the notation “ $\Delta$  mass loading”, which corresponds to  
347 the difference between the computed and the observed values of mass loading (in  $\text{kg}/\text{m}^2$ ). In  
348 the corresponding graphs (Figs. 3b, 4b, 5b and 6b)  $\Delta$  mass loading values (for each  
349 simulation) and observed mass loadings are reported for each section. A complete list of the  
350 stratigraphic sections employed is available in Table S3 from the Supporting information. We  
351 considered also the direction of the main elongation axis of the deposit by comparing isomass  
352 maps constructed from field data and those given by the model. With respect to mass loading  
353 values, additional parameters were also calculated to quantify the uncertainty of the model,  
354 which were: 1) the above-mentioned  $T^2$  function (see Section 2.2.1), which was normalized  
355 (for each eruption) by dividing it with the mean values of mass loading measured in the field  
356 (MML); 2) the percentage of sections for which there was an overestimation and an  
357 underestimation; 3) the mean overestimation (MO) and the mean underestimation (MU),

$$\begin{cases} MO = \frac{\sum_{i=1}^{N_o} \Delta_i}{N_o} \text{ for } \Delta_i > 0 \\ MU = \frac{\sum_{i=1}^{N_u} \Delta_i}{N_u} \text{ for } \Delta_i < 0 \end{cases}$$

358 where  $N_o$  and  $N_u$  are the number of sections with overestimation and underestimation,  
 359 respectively; 4) the respective ratios of MO and MU with the mean mass loading values  
 360 (MML) measured in the field.

361 With these four parameters the aim was to define, for each eruption and each meteo  
 362 data, 1) the discrepancy between the observed data and the model ( $T^2/\text{MML}$  – the  
 363 normalization allows to compare  $T^2$  from different eruptions), 2) whether the model tends  
 364 mostly to overestimate or underestimate the observed data (% of sections under or  
 365 overestimated), 3) the quantification of, respectively, the absolute model mean  
 366 underestimation (MU) and mean overestimation (MO) and, 4) how important are MO and  
 367 MU with respect to the mean values of mass loading measured in the field (MO/MML and  
 368 MU/MML ratios). Regarding the grain size data, instead, the modeled values of  $\text{Md}\phi$  or  $\sigma\phi$   
 369 were plotted as a function of the observed values at specific stratigraphic sections, and the  
 370 distribution of the data relative to a perfect fit line was discussed.

### 371 3. Results

372 For all the eruptions, Fig. 2 describes the stratigraphic sections used for uncertainty  
 373 quantification, Figs. 3-6 provide the results of each comparison, while Tables 2-5 summarize  
 374 the values calculated for each uncertainty quantification. Complementary data given in the  
 375 Supporting Information are: the output values (plume heights, mass loadings,  $\text{Md}\phi$  and  $\sigma\phi$   
 376 values, Tables S4-S7) and the simulation outputs in PDF (Figures S1-S16).

#### 377 3.1 Cotopaxi 2015

378 For the C15 eruption, a total of 35 mass loading measurements [from *Bernard et al.*,  
 379 2016a] and 4 grain size analyses [unpublished and from *Gaunt et al.*, 2016] were used for  
 380 comparison with our model (Fig. 2a).  
 381

382 For each meteo condition and for the values of MER considered, plume heights  
 383 comparison (Fig. 3a) shows that PLUME-MoM results are generally lower than those  
 384 obtained by inverting seismic signal or from satellite/video camera images, though the model  
 385 data mimic the patterns of observations. The difference between observed and modeled values  
 386 (Table 2) is ~435-480 m for the seismic signal and video camera images while it is ~1300-  
 387 1400 m for the satellite measurements. We note, however, a few exceptions. For the seismic-  
 388 derived data, exceptions are the days around the 23<sup>rd</sup> of September, where modeled plume  
 389 heights are systematically higher than the inferred ones. In contrast, Fig. 3a shows that there is  
 390 a very good correlation between modeled and observed plume heights estimated from video  
 391 recordings for the first phase of the eruption (August and beginning of September).  
 392

393 Ground deposits data show a difference of about 15°-20° between the directions of  
 394 modeled and observed main dispersal axes (Figs. 2a and 3b). Notice that the deposits  
 395 simulated, despite in extremely low quantities (i.e.  $10^{-10}$ - $10^{-11}$  kg/m<sup>2</sup>) at more distal locations,  
 396 are spread all over the computational domain (see Figs. S1 to S3). Mass loading data show  
 397 that the simulations underestimate field observations at locations in the main dispersal axes  
 398 (Fig. 3b). Notice that the two sections along the main dispersal axes with the highest  
 399 underestimations (BNAS and PNC 4 sections, see Table S3 from the Supporting Information)  
 400 have observed mass loading values of, respectively, 18 and 15 kg/m<sup>2</sup>; for these two sections,

401 which are very proximal (~5 and ~7 km from the vent respectively) the model predicts very  
 402 low deposition ( $<1 \text{ kg/m}^2$  for all the simulations). The  $T^2/\text{MML}$  values (Table 2) show that the  
 403 differences between model and observed values are relatively low, and the model generally  
 404 underestimates the observed values (57% to 77% of the field sections are underestimated). An  
 405 area of model underestimation might be recognized close to the vent area along the main  
 406 dispersal axes for all the simulations (see Figure S17 from the Supporting Information). The  
 407 MO and MU values (and also the MO/MML and MU/MML ratios) are similar for the  
 408 different meteo data, and for all the cases with a higher value of MU and MU/MML (for  
 409 simulations done using the NCEP/NCAR and the ERA-Interim meteo data).

410 The grain size data are scarce but we note that the computed  $\text{Md}\phi$  values are almost  
 411 always shifted toward coarser sizes (Fig. 3c) and that the  $\sigma\phi$  values show that the sorting of  
 412 the computed deposit is much smaller with respect to reality (Fig. 3d). Both computed  $\text{Md}\phi$   
 413 and  $\sigma\phi$  show nearly constant values for a given section but with different meteo data.

414

### 415 **3.2 Tungurahua 2013**

416 For the T13 eruption, a total of 48 mass loading measurements [unpublished and from  
 417 *Parra et al.*, 2016] and 29 grain size analyses [unpublished and from *Parra et al.*, 2016] were  
 418 used for the comparison (Fig. 2b).

419 The plume heights comparison (Fig. 4a) shows that all the simulations markedly  
 420 underestimate the observations reported from both sources. The mean difference is about -2.1  
 421 km to -2.2 km (Table 3). The difference of deposit main dispersal axes is small since the  
 422 simulations done using GDAS and ERA-Interim data are almost coincident with respect to  
 423 field data while the NCAR simulation is only  $8^\circ$  shifted toward the SW (Figs. 2b and 4b).

424 The observed values of mass loading (Fig. 4b and Table S3 from the Supporting  
 425 Information) are all  $<3 \text{ kg/m}^2$ , similarly with respect to the C15 eruption for the two sections  
 426 along the main dispersal axes (San Pedro de Sabanag and 12 de Octubre, Table S3 from the  
 427 Supporting Information). Mass loading differences have a small spread highlighted by low  
 428  $T^2/\text{MML}$  values (Table 3). This is also shown by the absolute differences (MO and MU),  
 429 which are also almost identical despite the model tends to underestimate field data at most  
 430 sections. For the T13 eruption, the distribution of sections with overestimation and  
 431 underestimation does not highlight homogeneous areas of model overestimation or  
 432 underestimation (see Fig. S18 from the Supporting Information). In Table 3 the MO/MML  
 433 and MU/MML ratios have both values  $<1$ , indicating that the difference in mass loading value  
 434 is less important than the average deposit value of mass loading. In Fig. 4b, the mass loading  
 435 differences with respect to the observed data are equally positive (overestimation) or negative  
 436 (underestimation) in proximity of the main dispersal axes, without a clear prevalence.

437 Grain size comparison highlights that, similarly to the C15 eruption, most of the  
 438 computed grain sizes are shifted toward constant coarser grained values ( $\text{Md}\phi$ , see Fig. 4c)  
 439 with a smaller and fairly constant sorting for much of the sections ( $\sigma\phi$ , see Fig. 4d). Notice,  
 440 however, that some simulation sorting values are along the perfect fit line (mostly  
 441 NCEP/NCAR simulation) or are even larger than the observed ones (GDAS and the ERA-  
 442 Interim simulations).

443

### 444 **3.3 Tungurahua 2006**

445 For the T06 eruption, a total of 48 mass loading measurements [*Eychenne et al.*, 2012]  
 446 and 22 grain size analyses [recalculated from *Eychenne et al.*, 2012, see also Text S1 from the  
 447 Supporting Information] were used for the comparison (Fig. 2c).

448 Fig. 5a shows that the plume heights simulated are close to observed data, except for  
 449 the NCEP/NCAR model. The ERA-Interim/WRF model, in particular, provides a low mean  
 450 overestimation of about 400 m (Table 4). Notice that this simulation was characterized by a  
 451 fairly low  $T^2$  value, although higher with respect to the parent ERA-Interim simulation (Table  
 452 4). This difference is due to the iterative procedure described in Section 2.4, which allowed  
 453 finding the hourly values of MERs that minimized the differences in plume heights. Another  
 454 combination of MERs was instead used for the other three meteorological datasets.  
 455 Differences in deposit main dispersal axes are the highest of the four studied eruptions and are  
 456 up to about  $40^\circ$  toward South (see ERA-Interim meteo in Figs. 2c and 5b).

457 With respect to mass loading, the  $T^2$ /MML values (Table 4) highlight a relatively high  
 458 spread of the data, which is also reflected in the MO and MU values. In this case, it could be  
 459 considered that most of the sections with underestimation are concentrated in proximity of the  
 460 main dispersal axis highlighted by field data (Fig. 5b). Notice that the NCEP/NCAR provides  
 461 the highest values of overestimation (MO = 62.57, MO/MML = 7.68). Moreover, the T06  
 462 eruption is one of the two cases, among the studied ones, where one simulation gives more  
 463 sections with overestimation than sections with underestimation (ERA-Interim/WRF, see  
 464 Table 4). Considering the spatial distribution of sections with overestimation and  
 465 underestimation (see Fig. S19 from the Supporting Information), then a homogeneous area of  
 466 model overestimation might be identified in the proximity of the vent area along the main  
 467 dispersal axes (see Fig. S19 from the Supporting Information). Figure 5b highlights an  
 468 interesting pattern for all the sections since the difference in mass loading tends to increase  
 469 approaching the main dispersal axis, which is particularly evident for the GDAS and the  
 470 NCEP/NCAR simulations.

471 The grain size data show a fairly well defined trend of  $Md\phi$  values, which are close to  
 472 the perfect fit line (Fig. 5c). The model sorting values are instead mostly shifted toward lower  
 473 values but define trends mimicking that of the perfect fit line (Fig. 5d).

474

### 475 **3.4 Puyehue-Cordón Caulle 2011**

476 For the PCC11 eruption, a total of 75 mass loading measurements and 24 grain size  
 477 analyses [Bonadonna *et al.*, 2015a; Pistolesi *et al.*, 2015; unpublished] were used for the  
 478 comparison (Fig. 2d). For the mass loadings, the thickness data of Pistolesi *et al.* [2015] were  
 479 multiplied by the bulk deposit density value of  $560 \text{ kg/m}^3$  reported in Bonadonna *et al.*  
 480 [2015a] for Unit I, in order to obtain  $\text{kg/m}^2$  values. Daily average plume heights a.s.l. reported  
 481 in Bonadonna *et al.* [2015b] have been converted into “above vent” values by subtracting the  
 482 vent elevation reported in Bonadonna *et al.* [2015b] (1470 m a.s.l.).

483 For this eruption, the simulations generally overestimate the plume heights observed,  
 484 which are lowered with the inverse procedure (see Table 5, Fig. 6a). The simulated deposit  
 485 main dispersal axes are all shifted toward the South by  $5\text{-}10^\circ$  with respect to the field data  
 486 (Figs. 2d and 6b).

487 For the mass loading, most of the  $T^2$ /MML values are the highest among all the  
 488 simulations, with values up to 22.12 (ERA-Interim) (Table 5). MO and MU values are  
 489 respectively  $>100 \text{ kg/m}^2$  and from  $-18 \text{ kg/m}^2$  up to  $-54 \text{ kg/m}^2$ . The MO/MML and MU/MML  
 490 ratios indicate anyway that mean overestimation is 3 to 6 times higher than MML and that  
 491 mean underestimation is 0.3 to 1 times higher than MML. As for the other eruptions, the  
 492 percentage of sections with overestimation is lower than that with underestimation, except for  
 493 the simulation done with the GDAS meteo data (Table 5). From Fig. S20 from the Supporting  
 494 Information, the distribution of the sections with overestimation or underestimation highlights  
 495 a homogeneous area of model overestimation located 30-40 km from vent area along the main  
 496 dispersal axes. The correlation between high values of mass loading overestimation and the

497 position of the main dispersal axis (Figure 6b) is evident only for the simulation done with the  
 498 ERA-Interim meteorological data. For the other simulations instead, the sections with the  
 499 highest differences are uncorrelated with respect to the position of the main dispersal axis  
 500 given by the model. It is also important to underline that in this case also, sections with  
 501 highest values of observed mass loadings are not correlated with the deposit main dispersal  
 502 axis given by field data, a pattern that is confirmed also by the simulations (see Fig. 6b). This  
 503 latter feature might be correlated with the progressive anticlockwise rotation of the ash cloud,  
 504 a pattern already discussed by *Pistolesi et al.* [2015] and *Bonadonna et al.* [2015b]. To  
 505 confirm this, we have also performed a more detailed analysis using satellite images to track  
 506 the evolution of the ash cloud during the 04-05/06/2011: details about this method are  
 507 reported in Text S1 from the Supporting Information. The sequence of images derived (Figure  
 508 S21 from the Supporting Information) show that at the onset of the eruption the cloud drifted  
 509 southwestwardly ( $130^\circ$ ), but as time passed, the cloud rapidly moved towards the east,  
 510 reaching  $105^\circ$ . This compares with the main dispersal axis assessed from the field deposits  
 511 integrated over the whole Unit I (layers A-F) and yielding a mean direction of  $117^\circ$ . However,  
 512 the maximum mass loading of deposits have been recorded at much higher angles, lying  
 513 between  $130\text{-}135^\circ$  (Figure 6b). This actually correlates with ash emissions occurring at the  
 514 onset of the eruption, where the ash-rich plume might have produced rapid and en masse  
 515 fallouts along the main ash cloud dispersal axis centered at  $130^\circ$  (Figure S21 from the  
 516 Supporting Information). This is supported by mass loading values of the deposits, which are  
 517 very high on the dispersal axis (green dots in Figure S21), ranging from  $481.6\text{kg/m}^2$  close to  
 518 the vent (section n° 57, Table S3 from the Supporting Information) to  $160\text{ kg/m}^2$  at a greater  
 519 distance. By contrast, the mass loading of samples located away from the dispersal axis (red  
 520 dots in Figure S21), shows much lower values of about  $5.6\text{ kg/m}^2$ , although being close to the  
 521 vent. Interestingly, section n° 57 is also the one that tends to have the highest value of  
 522 underestimations (up to  $-400\text{ kg/m}^2$ ).

523 Regarding the grain size data, the  $Md\phi$  values are spread on both sides of the perfect  
 524 fit line (Fig. 6c). The NCEP/NCAR simulations (both direct and inverse) tend to give finer  
 525 grained values with respect to the observed data. The sorting data tend to define two trends of  
 526 constant values of  $\sigma\phi \sim 0.5$  and  $\sim 2$ , and some model sorting values are higher than the  
 527 observed ones (Fig. 6d). An important remark for the modeled grain sizes of the PCC11  
 528 eruption is that none of them show any bimodal distribution in contrast to the observed data.  
 529 This is particularly evident for the above-mentioned section n° 57, which does not have  
 530 bimodality and which has an  $Md\phi$  shifted toward more coarser-grained values.

531

532

## 533 4. Discussion

### 534 4.1 Uncertainty in the input parameters

535 A significant amount of uncertainty in the simulations may derive from the  
 536 meteorological data employed. As also shown by other studies [e.g. *Devenish et al.*, 2012;  
 537 *Webster et al.*, 2012], even small errors in the wind field can lead to large errors in the ash  
 538 concentration, making therefore a point-by-point comparison of modelled with observed data  
 539 a challenging task. The datasets we considered are among the most widely used in similar  
 540 numerical modellings [e.g., *Webley et al.*, 2009; *Bonasia et al.*, 2012; *Folch*, 2012; *Costa et al.*  
 541 *et al.*, 2016]: moreover, it has also been used the mesoscale meteorological model WRF/ARW,  
 542 which has been coupled with other TTDMs in similar works [e.g. *FALL3D*, *Poret et al.*,  
 543 2017]. From our results, it is not evident that a particular meteorological dataset provides  
 544 systematically the best results. For instance, the GDAS dataset provides the worst results (in  
 545 terms of both the  $T^2$  and the MO-MU values) for the lower magnitude C15 and T13 eruptions,

546 while it provides the best results for the T06 and PCC11 eruptions. The NCEP/NCAR dataset  
547 shows the opposite as the results are better for the C15 and T13 eruptions with respect to T06  
548 and PCC11. The employment of the WRF/ARW model (see also Text S1 from the Supporting  
549 Information) did not result in a significant improvement of the results as it gave instead higher  
550  $T^2/\text{MML}$  values with respect to the parent ERA-Interim meteorological file (see Table 4),  
551 although for some other models the employment of the WRF/ARW model gave better results  
552 [Parra *et al.*, 2016]. Given the high computational times necessary to process original meteo  
553 data, the refinement procedure using WRF/ARW was not applied to other longer eruptions.  
554 The meteorological data have a considerable effect on the direction of main advection of the  
555 volcanic particles, which controls the deposit main dispersal axis direction. This is  
556 particularly evident for the T06 eruption, where differences with respect to the observed axis  
557 are up to  $40^\circ$ . Two main reasons for such differences may be invoked: i) the meteorological  
558 data are built in a way such that their parameters remain constant for relatively long periods (3  
559 to 6 hours) and for quite large areas ( $0.75^\circ \times 0.75^\circ$  up to  $2.5^\circ \times 2.5^\circ$ ), and within such temporal  
560 frames and spatial domains it is not possible to capture the variability of natural phenomena;  
561 ii) 4-dimensions meteorological files (especially Reanalysis products) might be less accurate  
562 over complex terrains (e.g. the Andes), for which the details of the atmospheric flow are less  
563 likely captured and there are not a lot of observations available. This could be the case for the  
564 T06 and T13 eruptions, where the rugged topography of the area surrounding the Tungurahua  
565 volcano could have caused secondary atmospheric effects not recorded in the meteorological  
566 files.

567 A common problem with eruption source parameters is the measurements of plume  
568 height. For instance, for the C15 eruption Bernard *et al.* [2016a] used three different  
569 methodologies for plume height estimates (inversion of seismic signals, video cameras  
570 observations, and satellite measurements), which gave sometimes very different values (see  
571 Fig. 3a). For the T06 eruption, Steffke *et al.* [2010] used two different methods of satellite  
572 observations. Therefore, it is not surprising that differences in measurements at the same time  
573 can be important. The uncertainty in plume height is also high for the T13 eruption, for which  
574 two different methods (satellite measurements and visual observations) have been employed,  
575 and for the PCC11 eruption as well, for which only daily mean values of plume height have  
576 been reported.

577 Mass loading values for the C15, T13 and T06 eruptions have been actually measured  
578 for each section (with various methods), but for the PCC11 they have been determined by  
579 multiplying the deposit thickness by a mean bulk deposit density value (see Section 3.4). This  
580 latter aspect is critical since density of tephra fall deposits may vary considerably owing to  
581 drastic density change between different particle sizes [e.g., Bonadonna and Phillips, 2003;  
582 Eychenne and Le Pennec, 2012; Pistolesi *et al.*, 2015]. This is particularly important for the  
583 PCC11 eruption that has the highest  $T^2/\text{MML}$  values (see Table 5), which might also be  
584 related to an uncertainty in the observed mass loading data. We also stress that the assumption  
585 of a linear variation of particle density with grain size (employed in PLUME-MoM) is a  
586 simplification since the density variation may be more complex [i.e sigmoidal rather than  
587 linear as for the T06 eruption, Eychenne and Le Pennec, 2012]. Compared to other sources of  
588 uncertainty, however, the simplification used in the simulations is expected to have a minor  
589 effect on the final results.

590 Finally, it is important to remark that there are also uncertainties in estimations of the  
591 initial water mass fraction in magmas. This is due primarily to the use of different methods  
592 [e.g., by direct measurements, geological inference, thermodynamic calculation or  
593 experimental approaches, see Clemens, 1984], among which the direct measurement from  
594 melt inclusions in crystals are the most used [see for example Plank *et al.*, 2013]. As a  
595 comparison, for this study we relied on estimates made both using direct measurements from

596 melt inclusions and experimental approaches [Martel et al., 2018] or considering only  
597 experimental approaches [Andújar et al., 2017]: results gave H<sub>2</sub>O wt. % ranging between 4-6  
598 wt. % and 6-8 wt. % for andesites and rhyolites respectively. As the water mass fraction has a  
599 strong influence on the plume height simulated with PLUME-MoM [see section 2.2.1 and  
600 also de'Michieli Vitturi et al., 2016], its careful estimation is therefore of primary importance.  
601

## 602 4.2 Uncertainty in the numerical modelling

603 When MER values obtained from total deposit measurements are used as input  
604 parameters, PLUME-MoM underestimates the plume height measurements for three out of  
605 four eruptions tested, and there may be two main reasons for that. First, as already discussed  
606 in the previous section, the measurements are in some specific cases uncertain. Second, the  
607 mass eruption rate, assumed to be equal to the total mass of deposit divided with the eruption  
608 duration, may be underestimated in some cases (e.g. the T06 eruption) since deposits of  
609 pyroclastic density currents are neglected, hence giving lower plume heights. We note,  
610 however, that the mean underestimations (and mean overestimations as well) of the model for  
611 each eruption are lower with respect to the uncertainty in observed data among different  
612 methods, and that in some cases (e.g. the T06 eruption) the refinement of the meteorological  
613 data using the WRF/ARW model can sensibly reduce the difference in plume height with  
614 respect to observed data.

615 The PLUME-MoM/HYSPLIT model tends generally to have more points  
616 underestimating the mass loading data (see Tables 2 to 5). However, if the absolute mean  
617 differences (MO and MU) and their ratios with mean values of mass loading (MO/MML and  
618 MU/MML) are considered, then model overestimation is systematically higher with respect to  
619 underestimation. For example, for the PCC11 eruption and for the simulation done using the  
620 ERA-Interim data, MO is almost 10 times higher than MU (Table 5). The high values of MO  
621 or MU and of their ratios with MML tend also to be higher for higher magnitude eruptions  
622 (e.g. T06 and PCC11): in this regard the inverse procedure reduces considerably the  
623 discrepancy between modeled and observed data as indicated for instance by the  $T^2/MML$   
624 value for the PCC11 eruption.

625 The problem of model uncertainty is further illustrated by the difference in mass  
626 loading with respect to the orientation of the stratigraphic section (Figs. 3b, 4b, 5b and 6b).  
627 There are two opposite situations since the deposit main dispersal axis coincides either with  
628 the lowest values of  $\Delta$  mass loading (highest underestimation, e.g. C15 eruption, Fig. 3b) or  
629 with the highest values of  $\Delta$  mass loading (highest overestimation, T06 eruption, Fig. 7b, and  
630 to a lesser extent T13 and PCC11 eruptions). This may be explained considering the advective  
631 and diffusive parts of the transport equation used [Folch, 2012]. While the mass seems to be  
632 correctly advected in the simulations (although with some deviation with respect to observed  
633 data), the equations of HYSPLIT related to turbulent diffusion do not appear to work  
634 efficiently, underestimating the horizontal diffusion and concentrating the mass close to the  
635 main dispersal axis of advection. A similar issue has been also encountered by Hurst and  
636 Davis [2017]. This may explain the above-mentioned mass loading underestimation or  
637 overestimation, which are possibly increased by the fact that the HYSPLIT model does not  
638 account for complex collective settling mechanisms of volcanic ash caused by aggregation,  
639 gravitational instabilities, diffusive convection, particle-particle interactions and wake-capture  
640 effects [Del Bello et al., 2017; Gouhier et al., 2019]. However, the problem of the effect of  
641 diffusion on volcanic plumes dispersal and therefore on particle sedimentation is complex  
642 [see for example Devenish et al., 2012]: a more rigorous study is therefore needed for  
643 HYSPLIT to investigate the influence of different available diffusion equations on final  
644 results.

645 The failure to take into account such mechanisms implies that the simulated finest-  
646 grained particles are transported much further than in reality. For instance, the C15 eruption  
647 has a particularly fine-grained TGSD [due also to its hydrovolcanic nature, *Bernard et al.*,  
648 2016a] (see Table S2 from the Supporting Information) so that the mass is transported all over  
649 the computational domain (see Figs. S1 to S3 from the Supporting Information). The case of  
650 the PCC11 eruption is similar since the TGSD is up to  $12\phi$ , and an estimated amount of  $\sim 5\%$   
651 of the erupted mass is transported out of the computational domain. While for this eruption  
652 the finest fraction of the volcanic clouds circumvented the Southern hemisphere and passed  
653 over the South of Australia [*Collini et al.*, 2013], it is possible that part of the fine ash did not  
654 deposit (see also the issue of grain size analyses in the following paragraph). In this context,  
655 the transport of material could have been at its maximum along the main dispersal axes, and  
656 therefore the degree of underestimation of mass loading at proximal-medial sites along  
657 dispersal axes is maximized as well.

658 Regarding the simulated grain size data, the  $Md\phi$  values are systematically coarser-  
659 grained for the C15 and T13 low magnitude eruptions while they are either coarser-grained or  
660 finer-grained for the PCC11 eruption. The shifting toward coarser-grained  $Md\phi$  values can be  
661 explained by the fact that HYSPLIT neglects the above-mentioned collective settling  
662 mechanisms of volcanic ash. For the eruptions where the amount of fine ash is higher (the  
663 C15, T13 eruptions and partially the PCC11 one), the fine ash is transported distally, hence  
664 causing coarser grain sizes in proximal to medial sections. Moreover, the model is not capable  
665 of reproducing the bimodality of grain size distribution observed, as for instance in the PCC11  
666 eruption. The  $\sigma\phi$  comparisons show that, instead, for most cases the modeled data tend to  
667 have a lower sorting value with respect to the observed ones. These results show that the  
668 employment of grain size data for model validation is less reliable with respect to mass  
669 loading data.

670 Four important issues should be considered to improve the coupled PLUME-  
671 MoM/HYSPLIT model in the context of tephra fallout hazard assessments and probabilistic  
672 hazard maps production. First, the meteorological dataset must be considered carefully since  
673 it controls strongly the plume height. Second, the amount of fine ash and the duration of the  
674 eruption seem to be more critical than the magnitude of the eruption for mass loading  
675 calculations, since the simulations of higher magnitude eruptions of short duration with lower  
676 wt% of fine particles (i.e. T06 eruption) are more accurate than simulations of lower  
677 magnitude eruptions with longer durations and a higher amount of fines (i.e. the C15 and  
678 T13). If the magnitude, the amount of fine particles and the duration of the eruption are high  
679 (i.e. the PCC11 eruption), then the model tends to overestimate the natural data. Third, for the  
680 above-mentioned reasons, we recommend to employ PLUME-MoM/HYSPLIT in its present  
681 configuration for the production of hazard maps related to higher magnitude eruptions (i.e.  
682 sub-Plinian or Plinian). This is supported by our simulations of such eruptions (i.e. T06 and  
683 PCC11), for which overestimation is much higher (in terms of mean absolute values) with  
684 respect to underestimation. This latter point is important in a context of hazard assessment  
685 since underestimation may be considered as less acceptable than overestimation. Moreover, it  
686 is also important to remind that: a) specifically for our test eruptions, the lower magnitude  
687 ones tend to have longer durations and are more difficult to model due to the very high  
688 variability of both the eruptions parameters and atmospheric conditions, which are less likely  
689 to be captured; b) the T06 and PCC11 eruptions are those for which modeled and observed  
690 plume heights are more similar. Fourth, the MO/MML and MU/MML ratios may be used to  
691 account for model uncertainty and to serve as a basis for calculating coefficients that allow the  
692 creation of probabilistic maps (from the point of view of mass loading) that quantify the  
693 model mean overestimation and underestimation. For this purpose, statistical techniques  
694 might be employed to correct the model by estimating its deviance from the observed data.

695 **5. Conclusions**

696 This paper presents the coupling of the PLUME-MoM model with a renewed version  
 697 of the HYSPLIT tephra dispersal model. These two coupled models have been tested against  
 698 four eruptions of different magnitudes and styles from three Andean volcanoes. A procedure  
 699 of uncertainty quantification has been applied by computing the differences between modeled  
 700 and observed data of plume height, mass loading and grain size (in terms of  $Md\phi$  and  $\sigma\phi$ ).  
 701 Four different meteorological datasets (GDAS, NCAR/NCEP, ERA-Interim, ERA-  
 702 Interim+WRF) have been tested as well. The main conclusions and future perspectives of this  
 703 uncertainty quantification are:

- 704 • None of the meteorological datasets tested produced systematically the best results  
 705 for all the eruptions. This implies that if a specific dataset is employed for  
 706 numerical modelling, its uncertainty (as quantified here) should be considered.
- 707 • The PLUME-MoM model tends to underestimate measured plume heights, except  
 708 for the eruption with the highest magnitude tested (i.e. PCC11). Though  
 709 underestimation might be related to uncertainties in plume height measurements  
 710 and input data (e.g. mass eruption rate and initial water mass fraction), we note  
 711 that for most of the cases we investigated the mean underestimations of the model  
 712 for each eruption were lower with respect to the uncertainty in observed data.
- 713 • The PLUME-MoM/HYSPLIT model tends generally to have more points  
 714 underestimating the mass loading data. If absolute mean differences are  
 715 considered, however, then overestimation is almost always higher than  
 716 underestimation. The distribution of sections with overestimation and  
 717 underestimation does not highlight systematically homogeneous areas of either  
 718 overestimation or underestimation.
- 719 • The advective part of the HYSPLIT model appears to work more efficiently than  
 720 the diffusive part. Moreover, the failure to take into account any collective settling  
 721 mechanisms of volcanic ash in HYSPLIT might cause important discrepancies  
 722 between observed and modeled data of mass loading and, above all, grain size  
 723 distributions.
- 724 • For the above-mentioned reasons, high amounts of fine particles might reduce the  
 725 accuracy of the model when simulating mass loading and grain size data.
- 726 • If the PLUME-MoM/HYSPLIT model is meant to be employed for hazard  
 727 assessment purposes, we recommend considering high magnitude eruptions (i.e.  
 728 sub-Plinian or Plinian) as target cases, and mass loading as primary parameter.
- 729 • Future developments of this project should consider the comparison of simulations  
 730 outputs with those from other models, in order to identify which model is best  
 731 suited for a specific eruption type

732 **Acknowledgements**

733 This research was financed by the French government IDEX-ISITE initiative 16-IDEX-0001  
 734 (CAP 20-25), the French Research Institute for Sustainable Development (IRD) in the context  
 735 of the Laboratoire Mixte International “Séismes et Volcans dans les Andes du Nord” and the  
 736 CNRS Tellus programme. Marco Pistolesi is warmly acknowledged for providing additional  
 737 unpublished data for the Puyehue-Cordón Caulle 2011 eruption. The authors are grateful to  
 738 Sandra Banson and Cèline Planche for the help in setting up the simulations with WRF. We  
 739 thank two anonymous reviewers for useful comments that improved the quality of the  
 740 manuscript, and we acknowledge as well the editorial handling provided by Nico Fournier  
 741 and Martha Savage.

742 Data supporting the analyses and conclusions presented in this study could be found in a  
 743 repository in the Figshare community with the following DOI:  
 744 <https://doi.org/10.6084/m9.figshare.10298036.v1>.

745

746 **References**

- 747 Andújar, J., C. Martel, M. Pichavant, P. Samaniego, B. Scaillet, and I. Molina, 2017,  
 748 Structure of the plumbing system at Tungurahua volcano, Ecuador: insights from  
 749 phase equilibrium experiments on July–August 2006 eruption products, *J. Petrol.*,  
 750 58(7), 1249-1278, doi: <https://doi.org/10.1093/petrology/egx054>.
- 751 Bellotti, F., L. Capra, D. Sarocchi, and M. D'Antonio, 2010, Geostatistics and multivariate  
 752 analysis as a tool to characterize volcanoclastic deposits: Application to Nevado de  
 753 Toluca volcano, Mexico, *J. Volcanol. Geoth. Res.*, 191(1-2), 117-128, doi:  
 754 <https://doi.org/10.1016/j.jvolgeores.2010.01.005>.
- 755 Bernard, B., J. Battaglia, A. Proaño, S. Hidalgo, F. Vásconez, S. Hernandez, and M. C. Ruiz,  
 756 2016a, Relationship between volcanic ash fallouts and seismic tremor: quantitative  
 757 assessment of the 2015 eruptive period at Cotopaxi volcano, Ecuador, *Bull. Volc.*,  
 758 78(11), doi: 10.1007/s00445-016-1077-5.
- 759 Bernard, J., K. Kelfoun, J. L. Le Pennec, and S. V. Vargas, 2014, Pyroclastic flow erosion and  
 760 bulking processes: comparing field-based vs. modeling results at Tungurahua volcano,  
 761 Ecuador, *Bull. Volc.*, 76(9), 858, doi: 10.1007/s00445-014-0858-y.
- 762 Bernard, J., J. Eycheenne, J. L. Le Pennec, and D. Narváez, 2016b, Mass budget partitioning  
 763 during explosive eruptions: insights from the 2006 paroxysm of Tungurahua volcano,  
 764 Ecuador, *Geochem. Geophys. Geosy.*, 17(8), 3224-3240, doi: 10.1002/2016GC006431.
- 765 Berrisford, P., D. Dee, P. Poli, R. Brugge, K. Fielding, M. Fuentes, P. Kallberg, S. Kobayashi,  
 766 S. Uppala, and A. Simmons, 2011, The ERA-Interim archive, version 2.0.
- 767 Biass, S., and C. Bonadonna, 2014, TOTGS: total grainsize distribution of tephra fallout:  
 768 <https://vhub.org/resources/3297>.
- 769 Biondi, R., A. K. Steiner, G. Kirchengast, H. Brenot, and T. Rieckh, 2017, Supporting the  
 770 detection and monitoring of volcanic clouds: A promising new application of Global  
 771 Navigation Satellite System radio occultation, *Adv. Sp. Res.*, 60(12), 2707-2722, doi:  
 772 <https://doi.org/10.1016/j.asr.2017.06.039>.
- 773 Bonadonna, C., and J. C. Phillips, 2003, Sedimentation from strong volcanic plumes, *J.*  
 774 *Geophys. Res.-Sol. Ea.*, 108(B7), 2340, doi: 10.1029/2002JB002034.
- 775 Bonadonna, C., R. Cioni, M. Pistolesi, M. Elissondo, and V. Baumann, 2015a, Sedimentation  
 776 of long-lasting wind-affected volcanic plumes: the example of the 2011 rhyolitic  
 777 Cordón Caulle eruption, Chile, *Bull. Volc.*, 77(2), doi: [https://doi.org/10.1007/s00445-](https://doi.org/10.1007/s00445-015-0900-8)  
 778 015-0900-8.
- 779 Bonadonna, C., M. Pistolesi, R. Cioni, W. Degruyter, M. Elissondo, and V. Baumann, 2015b,  
 780 Dynamics of wind-affected volcanic plumes: The example of the 2011 Cordón Caulle  
 781 eruption, Chile, *J. Geophys. Res.-Sol. Ea.*, 120(4), 2242-2261, doi:  
 782 10.1002/2014JB011478.
- 783 Bonasia, R., G. Macedonio, A. Costa, D. Mele, and R. Sulpizio, 2010, Numerical inversion  
 784 and analysis of tephra fallout deposits from the 472 AD sub-Plinian eruption at  
 785 Vesuvius (Italy) through a new best-fit procedure, *J. Volcanol. Geoth. Res.*, 189(3-4),  
 786 238-246, doi: <https://doi.org/10.1016/j.jvolgeores.2009.11.009>.
- 787 Bonasia, R., A. Costa, A. Folch, G. Macedonio, and L. Capra, 2012, Numerical simulation of  
 788 tephra transport and deposition of the 1982 El Chichón eruption and implications for

- 879 hazard assessment, *J. Volcanol. Geoth. Res.*, 231(2012), 39-49, doi:  
880 <https://doi.org/10.1016/j.jvolgeores.2012.04.006>.
- 891 Bursik, M. I., 2001, Effect of wind on the rise height of volcanic plumes, *Geophys. Res. Lett.*,  
892 28(18), 3621-3624, doi: <https://doi.org/10.1029/2001GL013393>.
- 893 Caballero, L., D. Sarocchi, E. Soto, and L. Borselli, 2014, Rheological changes induced by  
894 clast fragmentation in debris flows, *J. Geophys. Res.-Earth*, 119(9), 1800-1817, doi:  
895 [10.1002/2013JF002942](https://doi.org/10.1002/2013JF002942).
- 896 Clemens, J. D., 1984, Water contents of silicic to intermediate magmas, *Lithos*, 17(273-287),  
897 doi: [https://doi.org/10.1016/0024-4937\(84\)90025-2](https://doi.org/10.1016/0024-4937(84)90025-2).
- 898 Collini, E., M. S. Osores, A. Folch, J. G. Viramonte, G. Villarosa, and G. Salmuni, 2013,  
899 Volcanic ash forecast during the June 2011 Cordón Caulle eruption, *Nat. Hazards*,  
900 66(2), 389-412, doi: <https://doi.org/10.1007/s11069-012-0492-y>.
- 901 Connor, L. J., and C. B. Connor, 2006, Inversion is the key to dispersion: understanding  
902 eruption dynamics by inverting tephra fallout, in Mader, H. M., Coles, S.G., Connor,  
903 C.B., Connor, L.J, *Statistics in Volcanology*, IAVCEI Special Publication, The  
904 Geological Society of London, p. 231-241, doi:  
905 <https://doi.org/10.1144/IAVCEI001.18>.
- 906 Costa, A., F. Dell'Erba, M. A. Di Vito, R. Isaia, G. Macedonio, G. Orsi, and T. Pfeiffer, 2009,  
907 Tephra fallout hazard assessment at the Campi Flegrei caldera (Italy), *Bull. Volc.*,  
908 71(3), 259, doi: <https://doi.org/10.1007/s00445-008-0220-3>.
- 909 Costa, A., Y. J. Suzuki, M. Cerminara, B. J. Devenish, T. Esposti Ongaro, M. Herzog, A. R.  
910 Van Eaton, L. C. Denby, M. I. Bursik, M. de'Michieli Vitturi, S. Engwell, A. Neri, S.  
911 Barsotti, A. Folch, G. Macedonio, F. Girault, G. Carazzo, S. Tait, E. Kaminski, L. G.  
912 Mastin, M. J. Woodhouse, J. C. Phillips, A. J. Hogg, W. Degruyter, and C.  
913 Bonadonna, 2016, Results of the eruptive column model inter-comparison study, *J.*  
914 *Volcanol. Geoth. Res.*, 326(2016), 2-25, doi:  
915 <https://doi.org/10.1016/j.jvolgeores.2016.01.017>.
- 916 de'Michieli Vitturi, M., A. Neri, and S. Barsotti, 2015, PLUME-MoM 1.0: A new integral  
917 model of volcanic plumes based on the method of moments, *Geosci. Model Dev.*, 8(8),  
918 2447, doi: <https://doi.org/10.5194/gmd-8-2447-2015>.
- 919 de'Michieli Vitturi, M., S. L. Engwell, A. Neri, and S. Barsotti, 2016, Uncertainty  
920 quantification and sensitivity analysis of volcanic columns models: Results from the  
921 integral model PLUME-MoM, *J. Volcanol. Geoth. Res.*, 326(2016), 77-91, doi:  
922 <https://doi.org/10.1016/j.jvolgeores.2016.03.014>.
- 923 Dee, D. P., S. M. Uppala, A. J. Simmons, P. Berrisford, P. Poli, S. Kobayashi, U. Andrae, M.  
924 A. Balmaseda, G. Balsamo, and D. P. Bauer, 2011, The ERA-Interim reanalysis:  
925 Configuration and performance of the data assimilation system, *Q. J. Roy. Meteor.*  
926 *Soc.*, 137(656), 553-597, doi: <https://doi.org/10.1002/qj.828>.
- 927 Del Bello, E., J. Taddeucci, M. de' Michieli Vitturi, P. Scarlato, D. Andronico, S. Scollo, U.  
928 Kueppers, and T. Ricci, 2017, Effect of particle volume fraction on the settling  
929 velocity of volcanic ash particles: insights from joint experimental and numerical  
930 simulations, *Sci. Rep.-UK*, 7(39620), doi:  
931 <https://doi.org/10.1038/s41598-017-00000-0>.
- 932 Devenish, B. J., P. N. Francis, B. T. Johnson, R. S. J. Sparks, and D. J. Thomson, 2012,  
933 Sensitivity analysis of dispersion modeling of volcanic ash from Eyjafjallajökull in  
934 May 2010, *J. Geophys. Res.-Atmos.*, 117(D00U21), doi: [10.1029/2011JD016782](https://doi.org/10.1029/2011JD016782).
- 935 Douillet, G. A., È. Tsang-Hin-Sun, U. Kueppers, J. Letort, D. A. Pacheco, F. Goldstein, F.  
936 Von Aulock, Y. Lavallée, J. B. Hanson, and J. Bustillos, 2013, Sedimentology and  
937 geomorphology of the deposits from the August 2006 pyroclastic density currents at  
938 Tungurahua volcano, Ecuador, *Bull. Volc.*, 75(11), 765, doi:  
<https://doi.org/10.1007/s00445-013-0765-7>.

- 839 Engwell, S., and J. Eychenne, 2016, Contribution of fine ash to the atmosphere from plumes  
 840 associated with pyroclastic density currents, *Volcanic Ash*, Elsevier, p. 67-85, doi:  
 841 <https://doi.org/10.1016/B978-0-08-100405-0.00007-0>.
- 842 Eychenne, J., and J. L. Le Pennec, 2012, Sigmoidal particle density distribution in a  
 843 subplinian scoria fall deposit, *Bull. Volc.*, 74(10), 2243-2249, doi:  
 844 <https://doi.org/10.1007/s00445-012-0671-4>.
- 845 Eychenne, J., J. L. Le Pennec, L. Troncoso, M. Gouhier, and J. M. Nedelec, 2012, Causes and  
 846 consequences of bimodal grain-size distribution of tephra fall deposited during the  
 847 August 2006 Tungurahua eruption (Ecuador), *Bull. Volc.*, 74(1), 187-205, doi:  
 848 <https://doi.org/10.1007/s00445-011-0517-5>.
- 849 Eychenne, J., J. L. Le Pennec, P. Ramon, and H. Yepes, 2013, Dynamics of explosive  
 850 paroxysms at open-vent andesitic systems: high-resolution mass distribution analyses  
 851 of the 2006 Tungurahua fall deposit (Ecuador), *Ear. Pl. Sci. Lett.*, 361(343-355), doi:  
 852 <https://doi.org/10.1016/j.epsl.2012.11.002>.
- 853 Folch, A., A. Costa, and G. Macedonio, 2009, FALL3D: A computational model for transport  
 854 and deposition of volcanic ash, *Comp. & Geos.*, 35(6), 1334-1342, doi.
- 855 Folch, A., 2012, A review of tephra transport and dispersal models: evolution, current status,  
 856 and future perspectives, *J. Volcanol. Geoth. Res.*, 235(96-115), doi:  
 857 <https://doi.org/10.1016/j.jvolgeores.2012.05.020>.
- 858 Folch, A., A. Costa, and G. Macedonio, 2016, FPLUME-1.0: An integral volcanic plume  
 859 model accounting for ash aggregation, *Geosci. Model Dev.*, 9(431-450), doi:  
 860 [10.5194/gmd-9-431-2016](https://doi.org/10.5194/gmd-9-431-2016).
- 861 Folk, R. L., and W. C. Ward, 1957, Brazos River bar [Texas]; a study in the significance of  
 862 grain size parameters, *J. Sediment. Res.*, 27(1), 3-26, doi:  
 863 <https://doi.org/10.1306/74D70646-2B21-11D7-8648000102C1865D>.
- 864 García Moreno, J. D., 2016, Mapeo y determinación de parámetros físicos de las corrientes de  
 865 densidad piroclásticas producidas por el volcán Tungurahua producidas desde el 2006,  
 866 Tesis de Ingeniería: Escuela Politécnica Nacional, 152 p, doi:  
 867 <http://bibdigital.epn.edu.ec/handle/15000/15075>.
- 868 Gaunt, H. E., B. Bernard, S. Hidalgo, A. Proaño, H. Wright, P. A. Mothes, E. Criollo, and U.  
 869 Kueppers, 2016, Juvenile magma recognition and eruptive dynamics inferred from the  
 870 analysis of ash time series: the 2015 reawakening of Cotopaxi volcano, *J. Volcanol.*  
 871 *Geoth. Res.*, 328(2016), 134-146, doi:  
 872 <https://doi.org/10.1016/j.jvolgeores.2016.10.013>.
- 873 Gouhier, M., J. Eychenne, N. Azzaoui, A. Guillin, M. Deslandes, M. Poret, A. Costa, and P.  
 874 Husson, 2019, Low efficiency of large volcanic eruptions in transporting very fine ash  
 875 into the atmosphere, *Sci. Rep.-UK*, 9(1), 1449, doi: <https://doi.org/10.1038/s41598-019-38595-7>.
- 877 Hall, M. L., A. L. Steele, P. A. Mothes, and M. C. Ruiz, 2013, Pyroclastic density currents  
 878 (PDC) of the 16–17 August 2006 eruptions of Tungurahua volcano, Ecuador:  
 879 Geophysical registry and characteristics, *J. Volcanol. Geoth. Res.*, 265(2013), 78-93,  
 880 doi: <https://doi.org/10.1016/j.jvolgeores.2013.08.011>.
- 881 Hidalgo, S., J. Battaglia, S. Arellano, A. L. Steele, B. Bernard, J. Bourquin, B. Galle, S.  
 882 Arrais, and F. Vásquez, 2015, SO<sub>2</sub> degassing at Tungurahua volcano (Ecuador)  
 883 between 2007 and 2013: Transition from continuous to episodic activity, *J. Volcanol.*  
 884 *Geoth. Res.*, 298(1-14), doi: <https://doi.org/10.1016/j.jvolgeores.2015.03.022>.
- 885 Hidalgo, S., J. Battaglia, S. Arellano, D. Sierra, B. Bernard, R. Parra, P. Kelly, F. Dinger, C.  
 886 Barrington, and P. Samaniego, 2018, Evolution of the 2015 Cotopaxi eruption  
 887 revealed by combined geochemical and seismic observations, *Geochem. Geophys.*  
 888 *Geosy.*, 19(7), 2087-2108, doi: <https://doi.org/10.1029/2018GC007514>.

- 889 Hurst, T., and C. Davis, 2017, Forecasting volcanic ash deposition using HYSPLIT, *J. Appl.*  
890 *Volcan.*, 6(1), 5, doi: <https://doi.org/10.1186/s13617-017-0056-7>.
- 891 Jay, J., F. Costa, M. Pritchard, L. Lara, B. Singer, and J. Herrin, 2014, Locating magma  
892 reservoirs using InSAR and petrology before and during the 2011–2012 Cordón  
893 Cauille silicic eruption, *Ear. Pl. Sci. Lett.*, 395(2014), 254-266, doi:  
894 <https://doi.org/10.1016/j.epsl.2014.03.046>.
- 895 Kalnay, E., M. Kanamitsu, R. Kistler, W. Collins, D. Deaven, L. Gandin, M. Iredell, S. Saha,  
896 G. White, J. Woollen, Y. Zhu, M. Chelliah, W. Ebisuzaki, W. Higgins, J. Janowiak, K.  
897 C. Mo, C. Ropelewski, J. Wang, A. Leetmaa, R. Reynolds, R. Jenne, and D. Joseph,  
898 1996, The NCEP/NCAR 40-Year Reanalysis Project, *Bull. Am. Met. Soc.*, 77(3), 437-  
899 472, doi: 10.1175/1520-0477(1996)077<0437:tnyrp>2.0.co;2.
- 900 Kelfoun, K., P. Samaniego, P. Palacios, and D. Barba, 2009, Testing the suitability of  
901 frictional behaviour for pyroclastic flow simulation by comparison with a well-  
902 constrained eruption at Tungurahua volcano (Ecuador), *Bull. Volc.*, 71(9), 1057, doi:  
903 <https://doi.org/10.1007/s00445-009-0286-6>.
- 904 Martel, C., J. Andújar, P. Mothes, B. Scaillet, M. Pichavant, and I. Molina, 2018, Storage  
905 conditions of the mafic and silicic magmas at Cotopaxi, Ecuador, *J. Volcanol. Geoth.*  
906 *Res.*, 354(74-86), doi: <https://doi.org/10.1016/j.jvolgeores.2018.02.006>.
- 907 Marti, A., A. Folch, O. Jorba, and Z. Janjic, 2017, Volcanic ash modeling with the online  
908 NMMB-MONARCH-ASH v1. 0 model: model description, case simulation, and  
909 evaluation, *Atmos. Chem. Phys.*, 17(2017), 4005-4030, doi: 10.5194/acp-17-4005-  
910 2017.
- 911 Michalakes, J., S. Chen, J. Dudhia, L. Hart, J. Klemp, J. Middlecoff, and W. Skamarock,  
912 2001, Development of a next-generation regional weather research and forecast  
913 model, *Developments in Teracomputing*, World Scientific, p. 269-276, doi:  
914 [https://doi.org/10.1142/9789812799685\\_0024](https://doi.org/10.1142/9789812799685_0024).
- 915 NOAA, 2004, Global Data Assimilation System (GDAS1) Archive Information.
- 916 Parra, R., B. Bernard, D. Narváez, J. L. Le Penneç, N. Hasselle, and A. Folch, 2016, Eruption  
917 Source Parameters for forecasting ash dispersion and deposition from vulcanian  
918 eruptions at Tungurahua volcano: Insights from field data from the July 2013 eruption,  
919 *J. Volcanol. Geoth. Res.*, 309(2016), 1-13, doi:  
920 <https://doi.org/10.1016/j.jvolgeores.2015.11.001>.
- 921 Pistolesi, M., R. Cioni, C. Bonadonna, M. Elissondo, V. Baumann, A. Bertagnini, L. Chiari,  
922 R. Gonzales, M. Rosi, and L. Francalanci, 2015, Complex dynamics of small-  
923 moderate volcanic events: the example of the 2011 rhyolitic Cordón Cauille eruption,  
924 Chile, *Bull. Volc.*, 77(1), 3, doi: <https://doi.org/10.1007/s00445-014-0898-3>.
- 925 Plank, T., K. A. Kelley, M. M. Zimmer, E. H. Hauri, and P. J. Wallace, 2013, Why do mafic  
926 arc magmas contain 4 wt% water on average?, *Ear. Pl. Sci. Lett.*, 364(168-179), doi:  
927 <https://doi.org/10.1016/j.epsl.2012.11.044>.
- 928 Poret, M., A. Costa, A. Folch, and A. Martí, 2017, Modelling tephra dispersal and ash  
929 aggregation: The 26th April 1979 eruption, La Soufrière St. Vincent, *J. Volcanol.*  
930 *Geoth. Res.*, 347(2017), 207-220, doi:  
931 <https://doi.org/10.1016/j.jvolgeores.2017.09.012>.
- 932 Riley, C. M., W. I. Rose, and G. J. S. Bluth, 2003, Quantitative shape measurements of distal  
933 volcanic ash, *J. Geophys. Res.-Sol. Ea.*, 108(B10), doi:  
934 <https://doi.org/10.1029/2001JB000818>.
- 935 Samaniego, P., J. L. Le Penneç, C. Robin, and S. Hidalgo, 2011, Petrological analysis of the  
936 pre-eruptive magmatic process prior to the 2006 explosive eruptions at Tungurahua  
937 volcano (Ecuador), *J. Volcanol. Geoth. Res.*, 199(1-2), 69-84, doi:  
938 <https://doi.org/10.1016/j.jvolgeores.2010.10.010>.

- 939 Scollo, S., A. Folch, and A. Costa, 2008, A parametric and comparative study of different  
940 tephra fallout models, *J. Volcanol. Geoth. Res.*, 176(2), 199-211, doi:  
941 <https://doi.org/10.1016/j.jvolgeores.2008.04.002>.
- 942 Skamarock, W. C., and J. B. Klemp, 2008, A time-split nonhydrostatic atmospheric model for  
943 weather research and forecasting applications, *J. Comput. Phys.*, 227(7), 3465-3485,  
944 doi: <https://doi.org/10.1016/j.jcp.2007.01.037>.
- 945 Steffke, A. M., D. Fee, M. Garces, and A. Harris, 2010, Eruption chronologies, plume heights  
946 and eruption styles at Tungurahua Volcano: Integrating remote sensing techniques and  
947 infrasound, *J. Volcanol. Geoth. Res.*, 193(3-4), 143-160, doi:  
948 <https://doi.org/10.1016/j.jvolgeores.2010.03.004>.
- 949 Stein, A. F., R. R. Draxler, G. D. Rolph, B. J. B. Stunder, M. D. Cohen, and F. Ngan, 2015,  
950 NOAA's HYSPLIT atmospheric transport and dispersion modeling system, *Bull. Am.*  
951 *Met. Soc.*, 96(12), 2059-2077, doi: <https://doi.org/10.1175/BAMS-D-14-00110.1>.
- 952 Tuffen, H., M. R. James, J. M. Castro, and C. I. Schipper, 2013, Exceptional mobility of an  
953 advancing rhyolitic obsidian flow at Cordón Caulle volcano in Chile, *Nat. Commun.*,  
954 4(2013), 2709, doi: <https://doi.org/10.1038/ncomms3709>.
- 955 Webley, P. W., B. J. B. Stunder, and K. G. Dean, 2009, Preliminary sensitivity study of  
956 eruption source parameters for operational volcanic ash cloud transport and dispersion  
957 models—A case study of the August 1992 eruption of the Crater Peak vent, Mount  
958 Spurr, Alaska, *J. Volcanol. Geoth. Res.*, 186(1-2), 108-119, doi:  
959 <https://doi.org/10.1016/j.jvolgeores.2009.02.012>.
- 960 Webster, H. N., D. J. Thomson, B. T. Johnson, I. P. C. Heard, K. Turnbull, F. Marenco, N. I.  
961 Kristiansen, J. Dorsey, A. Minikin, B. Weinzierl, U. Schumann, R. S. J. Sparks, S. C.  
962 Loughlin, M. C. Hort, S. J. Leadbetter, B. J. Devenish, A. J. Manning, C. S. Witham,  
963 J. M. Haywood, and B. W. Golding, 2012, Operational prediction of ash  
964 concentrations in the distal volcanic cloud from the 2010 Eyjafjallajökull eruption, *J.*  
965 *Geophys. Res.-Atmos.*, 117(D00U08), doi: 10.1029/2011JD016790.
- 966 Wilson, L., and T. C. Huang, 1979, The influence of shape on the atmospheric settling  
967 velocity of volcanic ash particles, *Ear. Pl. Sci. Lett.*, 44(2), 311-324, doi:  
968 [https://doi.org/10.1016/0012-821X\(79\)90179-1](https://doi.org/10.1016/0012-821X(79)90179-1).

969

970

971

972

973

974

975

976

977

978

979

980

981

982  
983  
984  
985  
986  
987  
988  
989  
990  
991  
992  
993  
994  
995  
996  
997

#### FIGURE CAPTIONS

998 **Figure 1.** Geographical locations of a) Cotopaxi and Tungurahua volcanoes in Ecuador and b)  
999 Puyehue-Cordón Caulle volcanic complex in Chile. Coordinates are in the UTM WGS84 17S  
1000 (a) and UTM WGS84 19S (b) systems. Basemap copyright of ESRI®, DigitalGlobe, GeoEye,  
1001 Earthstar Geographics, CNES/Airbus DS, USDA, USGS, AeroGRID, IGN, and the GIS User  
1002 Community.

1003  
1004 **Figure 2.** Stratigraphic sections used for uncertainty quantification (considering only mass  
1005 loading or both mass loading and grain size) and dispersal axes from field data/simulations  
1006 with different meteo data for: a) Cotopaxi C15 eruption; b) Tungurahua T13 eruption; c)  
1007 Tungurahua T06 eruption; d) Puyehue-Cordón Caulle PCC11 eruption. Digital Elevation  
1008 Model (30 m- resolution) from Marc Souris, IRD (a-c) and ESRI, USGS, NOAA (d).  
1009 Coordinates are in UTM WGS84 17S (a-c) and UTM WGS84 19S (d).

1010  
1011 **Figure 3.** Cotopaxi C15 eruption. Comparison of a) column height (observed and computed);  
1012 b)  $\Delta$  mass loading (left axis) and observed mass loading (right axis) for different sections with  
1013 respect to their orientation from North; c)  $Md\phi$  and d)  $\sigma\phi$  (computed and observed).

1014  
1015 **Figure 4.** Tungurahua T13 eruption. a) Column height (observed and computed); b)  $\Delta$  mass  
1016 loading (left axis) and observed mass loading (right axis) for different sections with respect to  
1017 their orientation from North; c)  $Md\phi$  and d)  $\sigma\phi$  (computed and observed).

1018

1019 **Figure 5.** Tungurahua T06 eruption. a) column height (observed and computed); b)  $\Delta$  mass  
 1020 loading (left axis) and observed mass loading (right axis) for different sections with respect to  
 1021 their orientation from North; c)  $Md\phi$  and d)  $\sigma\phi$  (computed and observed).

1022

1023 **Figure 6.** Puyehue-Cordón Caulle PCC11 eruption. a) Column height (observed and  
 1024 modeled); b)  $\Delta$  mass loading (left axis) and observed mass loading (right axis) for different  
 1025 sections with respect to their orientation from North; c)  $Md\phi$  and d)  $\sigma\phi$  (computed and  
 1026 observed).

1027

1028

1029

1030

1031

1032

1033

1034

## 1035 TABLES

1036

Eruption name	Computational grid dimension (°)	Initial water content (wt%)	Particles exit velocity (m/s)	Heat capacity (J/kg×K)	Particles Shape Factor	$\phi_1$	$\rho_1$ (kg/m <sup>3</sup> )	$\phi_2$	$\rho_2$ (kg/m <sup>3</sup> )
Cotopaxi 2015 (C15)	5x5	5.5%	135	1600	0.75	-1	1487	2	2478
Tungurahua 2013 (T13)	6 x 6	5.5%	135	1600	0.75	-1	1487	2	2478
Tungurahua 2006 (T06)	6 x 6	5.5%	275	1600	0.75	-1	1487	2	2478
Puyehue-Cordón Caulle 2011 (PCC11)	10 x 10	7.0%	275	1600	0.65	-4	500	5	2670

1037 **Table 1.** Main input parameters used for the simulations.

1038

Parameters	Meteo Data		
	GDAS	NCEP/NCAR	ERA-Interim
<i>PLUME-MoM</i>			
Mean Difference seismic (m)	-479.02	-443.75	-454.83
Mean Difference video (m)	-466.24	-434.99	-443.23
Mean Difference satellite (m)	-1449.64	-1405.96	-1366.64
<i>HYSPLIT</i>			
T <sup>2</sup> /MML	1.00	0.85	0.93
% Section Overestimation	42.9%	25.7%	22.9%

<b>% Section Underestimation</b>	57.1%	74.3%	77.1%
<b>MO (kg/m<sup>2</sup>)</b>	0.47	0.09	0.25
<b>MU (kg/m<sup>2</sup>)</b>	-3.04	-2.66	-2.60
<b>MO/MML</b>	0.21	0.04	0.11
<b>MU/MML</b>	-1.37	-1.20	-1.18

1039 **Table 2.** Values calculated for the uncertainty quantification for the C15 eruption.

1040

Parameters	Meteo Data		
	GDAS	NCEP/NCAR	ERA-Interim
<i>PLUME-MoM</i>			
<b>Mean Difference (m)</b>	-2202.05	-2113.75	-2132.03
<i>HYSPLIT</i>			
<b>T<sup>2</sup>/MML</b>	0.71	1.02	1.49
<b>% Section Overestimation</b>	29.2%	33.3%	35.4%
<b>% Section Underestimation</b>	70.8%	66.7%	64.6%
<b>MO (kg/m<sup>2</sup>)</b>	0.15	0.38	0.40
<b>MU (kg/m<sup>2</sup>)</b>	-0.47	-0.34	-0.37
<b>MO/MML</b>	0.28	0.75	0.77
<b>MU/MML</b>	-0.92	-0.67	-0.73

1041 **Table 3.** Values calculated for the uncertainty quantification for the T13 eruption.

1042

Parameters	Meteo Data			
	GDAS	NCEP/NCAR	ERA-Interim	ERA-Interim/WRF
<i>PLUME-MoM</i>				
<b>Mean Difference (m)</b>	-718.67	-3752.59	-1225.72	404.74
<i>HYSPLIT</i>				
<b>T<sup>2</sup>/MML</b>	5.41	19.67	1.78	4.59
<b>% Section Overestimation</b>	39.5%	44.2%	27.9%	55.8%
<b>% Section Underestimation</b>	60.5%	55.8%	72.1%	44.2%
<b>MO (kg/m<sup>2</sup>)</b>	23.96	62.57	15.64	19.73
<b>MU (kg/m<sup>2</sup>)</b>	-3.32	-2.74	-4.40	-2.88
<b>MO/MML</b>	2.94	7.68	1.92	2.42
<b>MU/MML</b>	-0.41	-0.34	-0.54	-0.35

1043 **Table 4.** Values calculated for the uncertainty quantification for the T06 eruption.

1044

Parameters	Meteo Data					
	GDAS	NCEP/NCAR	ERA-Interim	GDAS (inversion)	NCEP/NCAR (inversion)	ERA-Interim (inversion)
<i>PLUME-MoM</i>						
<b>Mean Difference (m)</b>	296.11	71.79	182.06	195.51	-84.86	33.27
<i>HYSPLIT</i>						
<b>T<sup>2</sup>/MML</b>	17.05	9.69	22.12	11.73	8.08	7.08
<b>% Section Overestimation</b>	50.7%	30.7%	34.7%	48.0%	32.0%	38.7%
<b>% Section Underestimation</b>	49.3%	69.3%	65.3%	52.0%	68.0%	61.3%
<b>MO (kg/m<sup>2</sup>)</b>	165.27	227.60	309.99	133.10	184.06	156.82
<b>MU (kg/m<sup>2</sup>)</b>	-53.93	-15.57	-31.94	-50.57	-18.72	-36.37
<b>MO/MML</b>	3.15	4.34	5.91	2.54	3.51	2.99
<b>MU/MML</b>	-1.03	-0.30	-0.61	-0.96	-0.36	-0.69

1045 **Table 5.** Values calculated for the uncertainty quantification for the PCC11 eruption.

**Figure 1.**

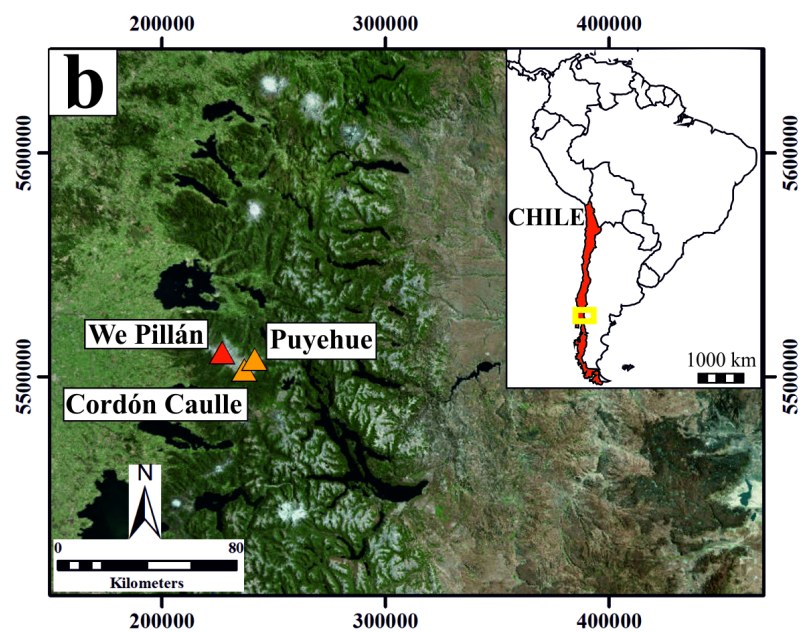
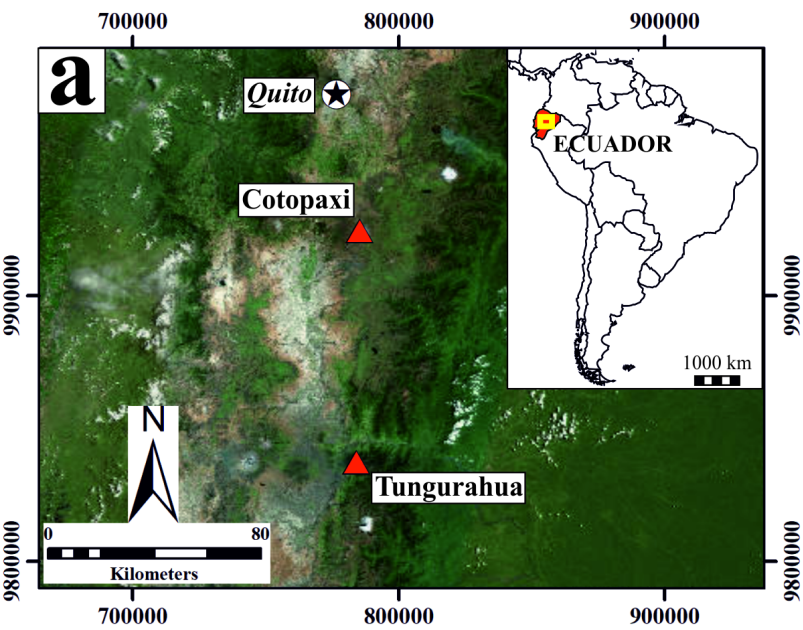


Figure 2.

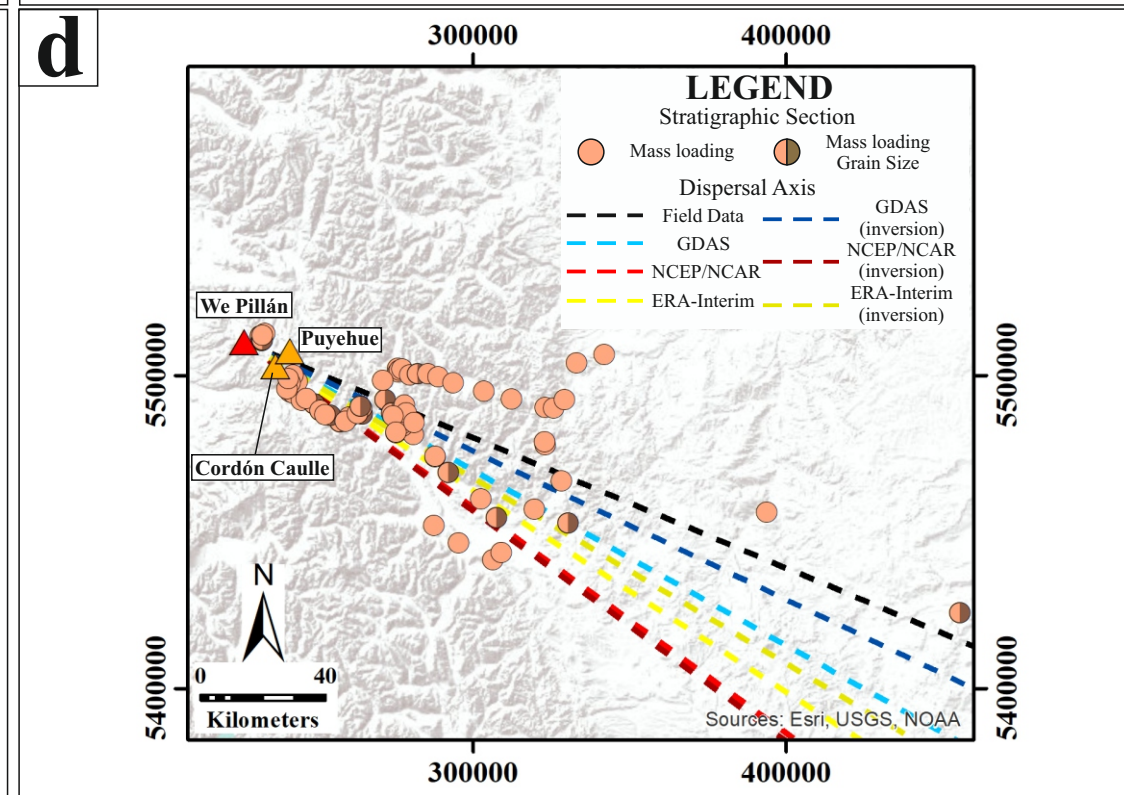
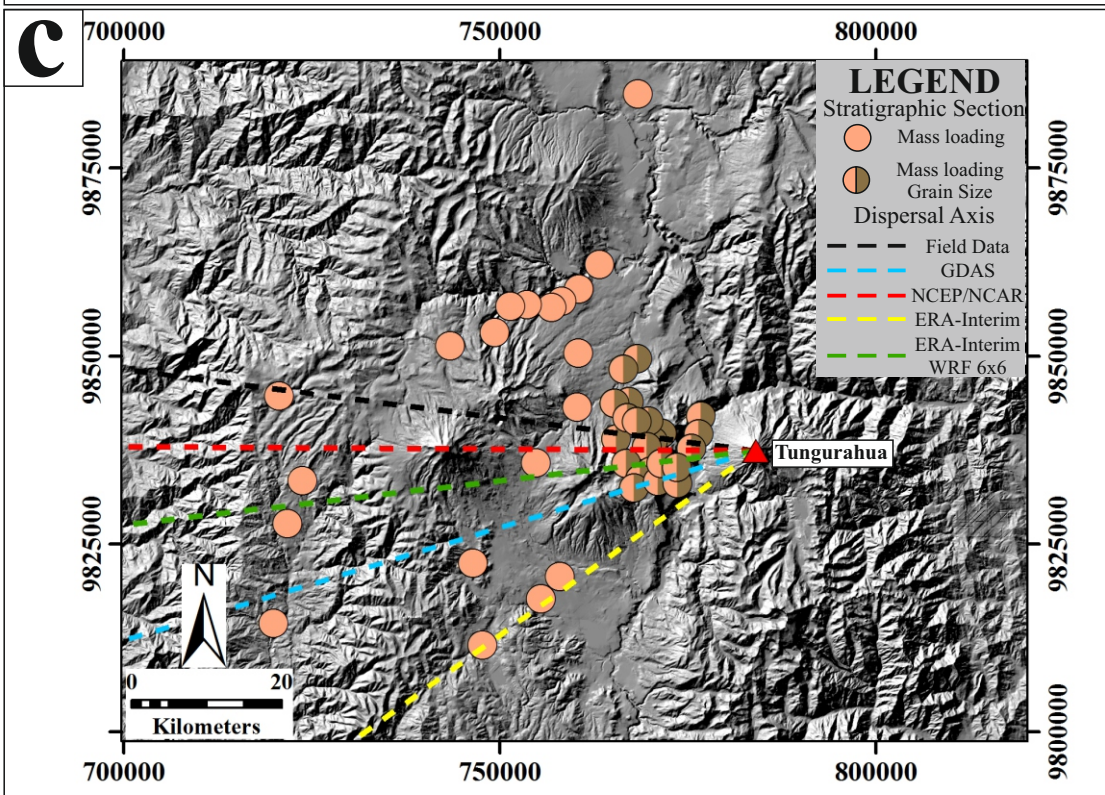
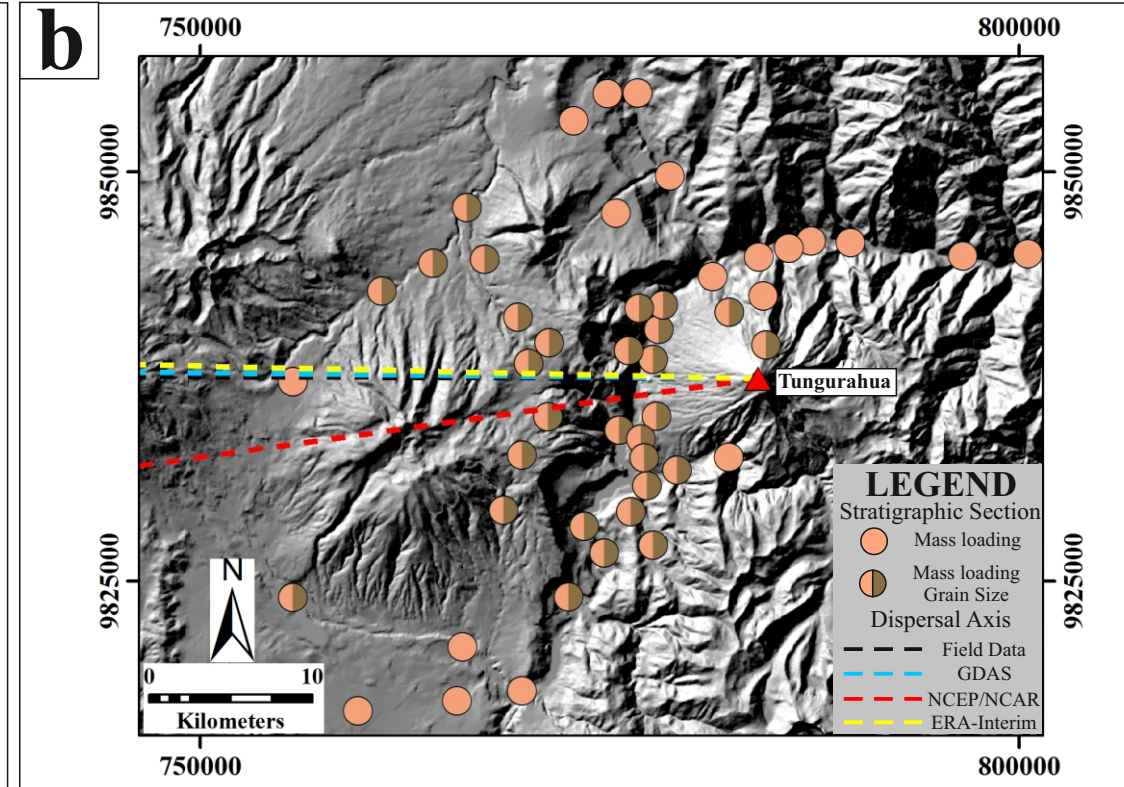
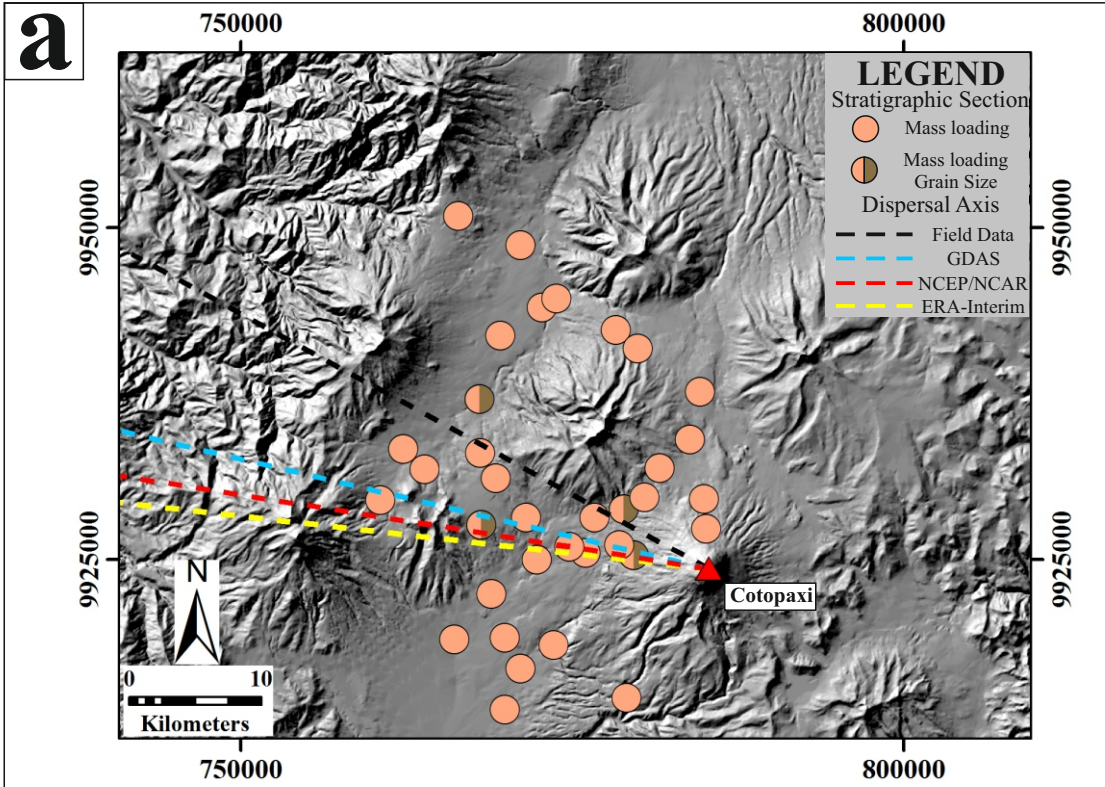
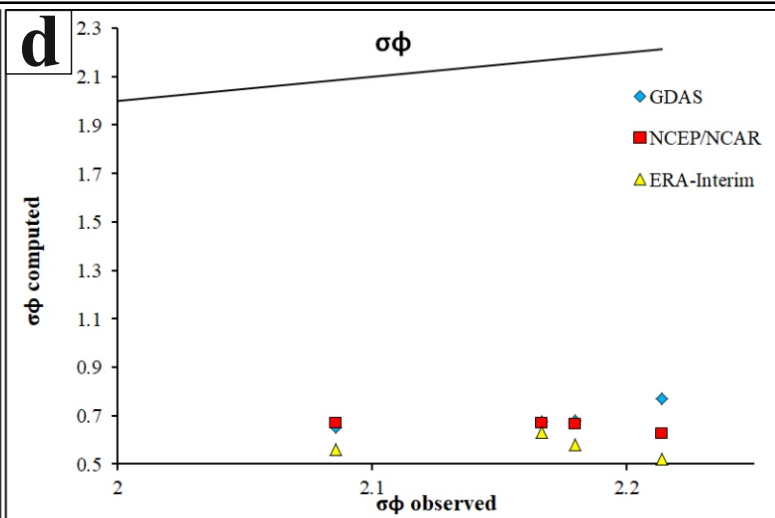
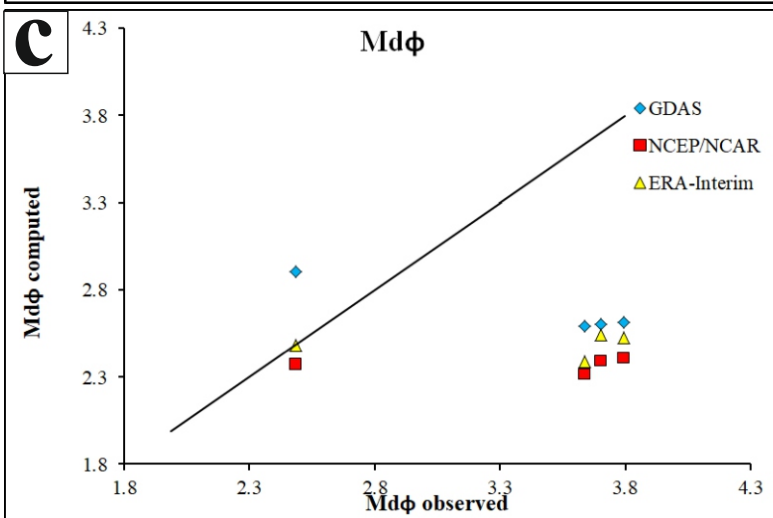
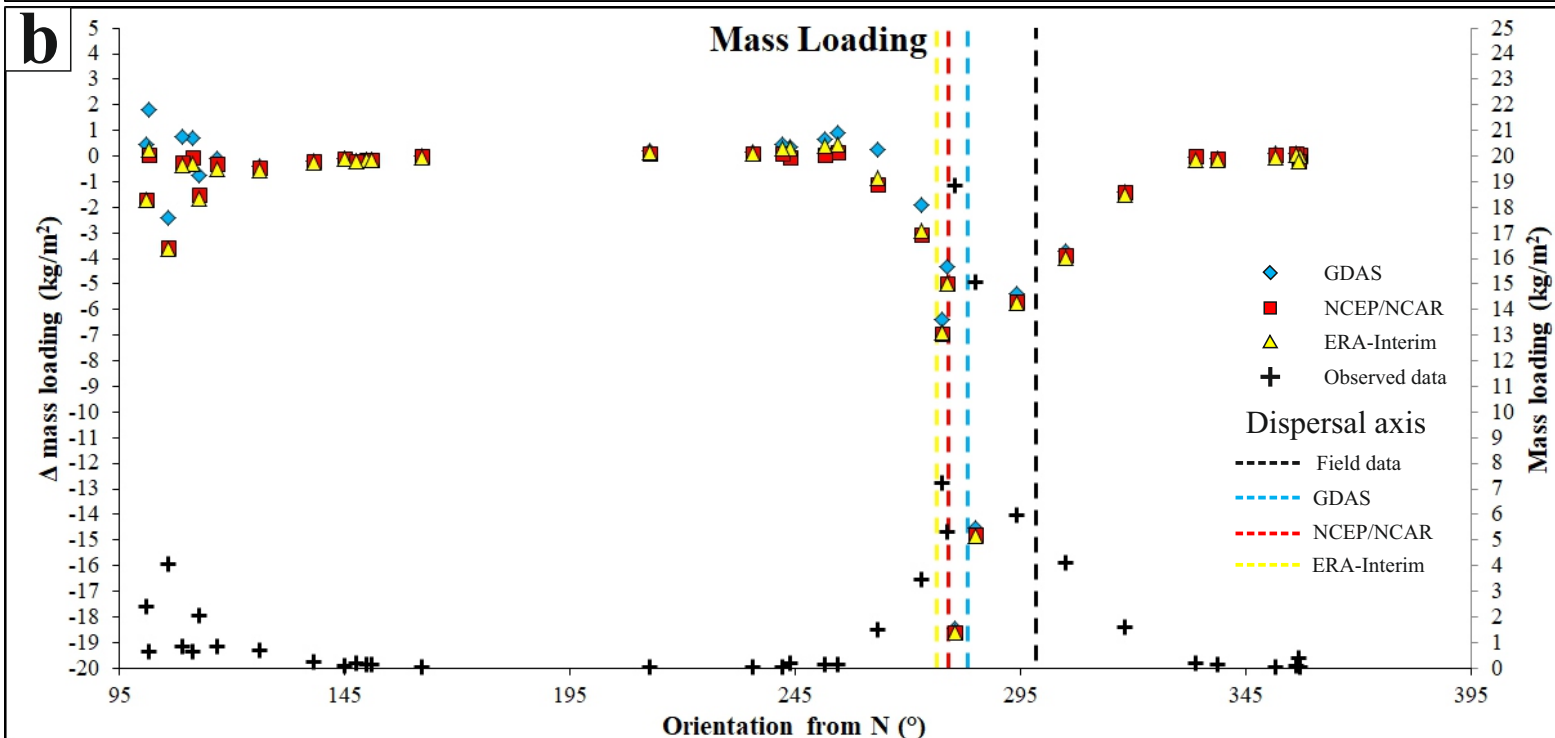
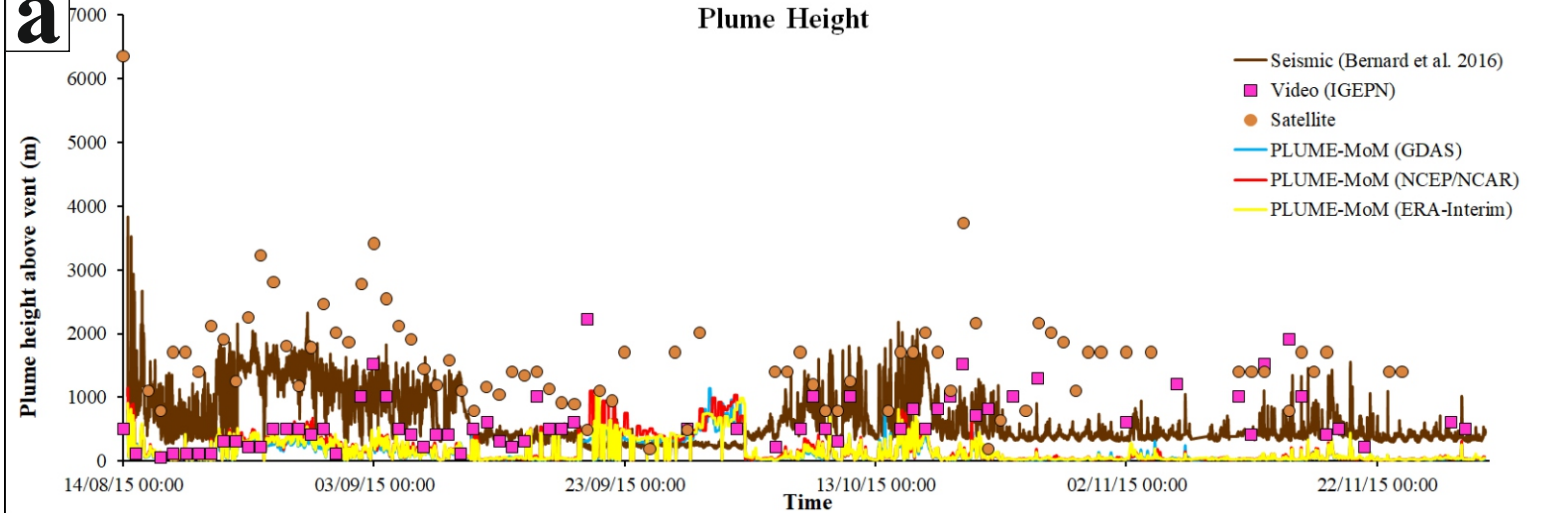
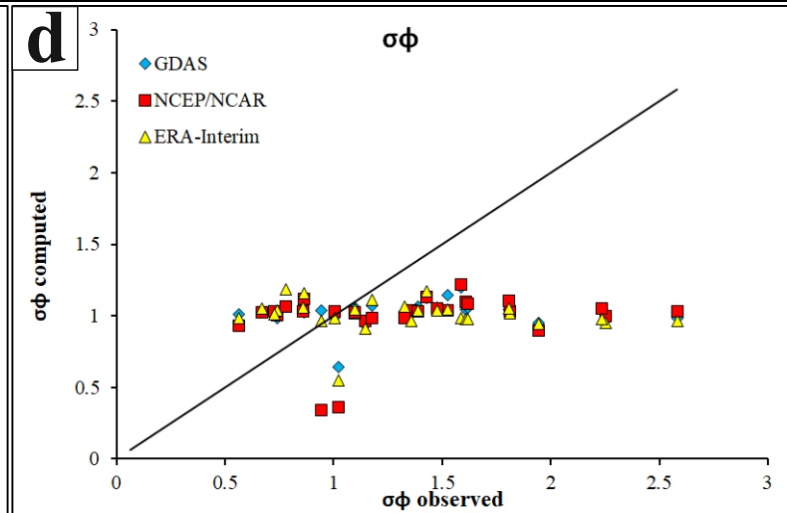
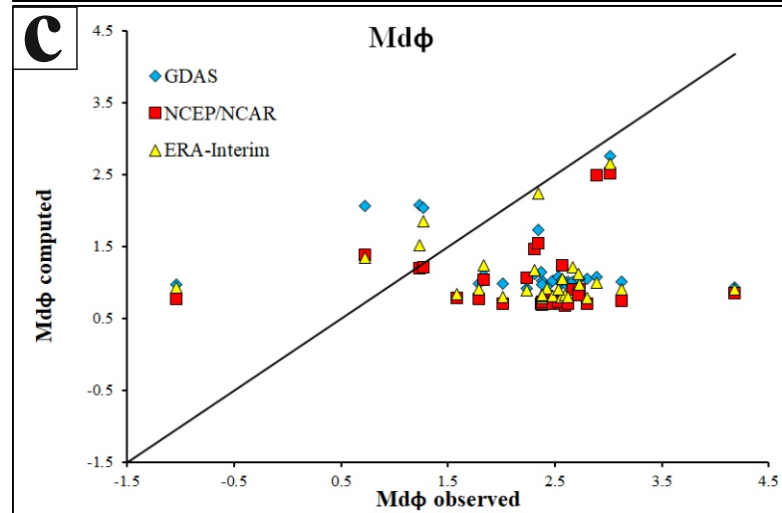
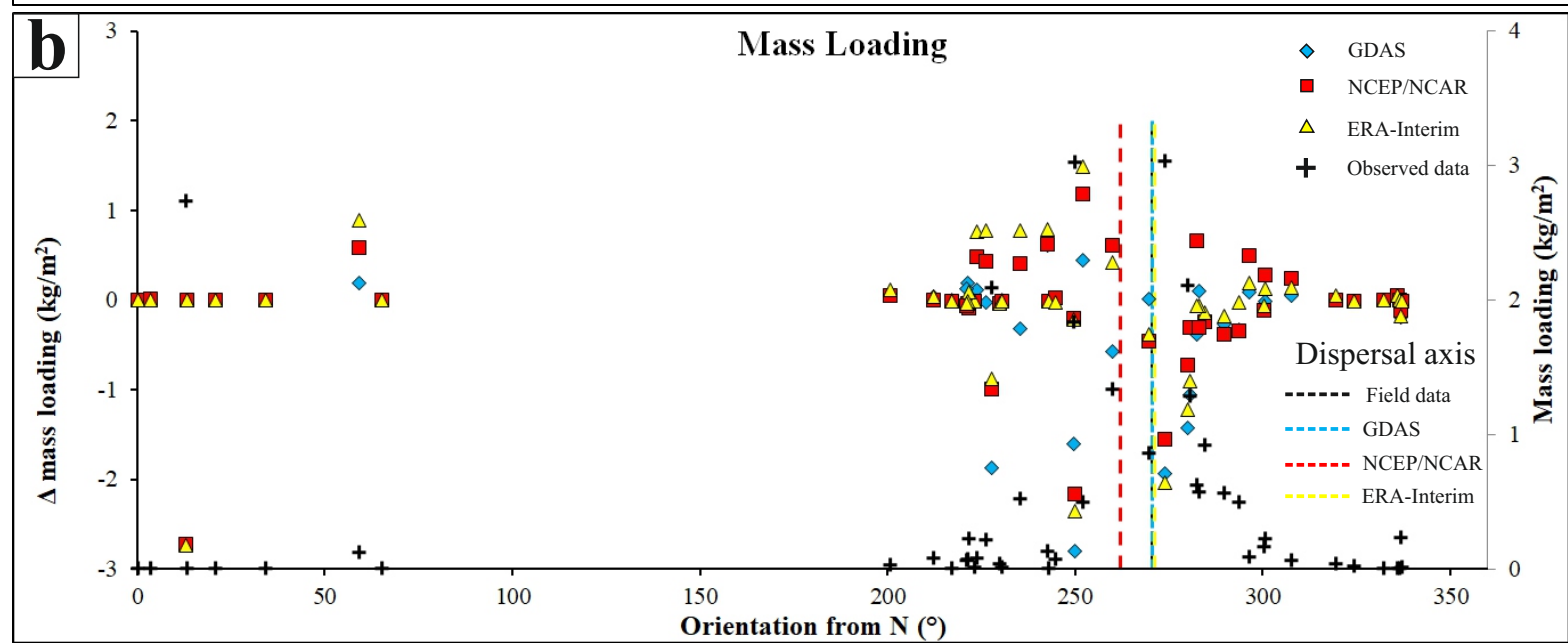
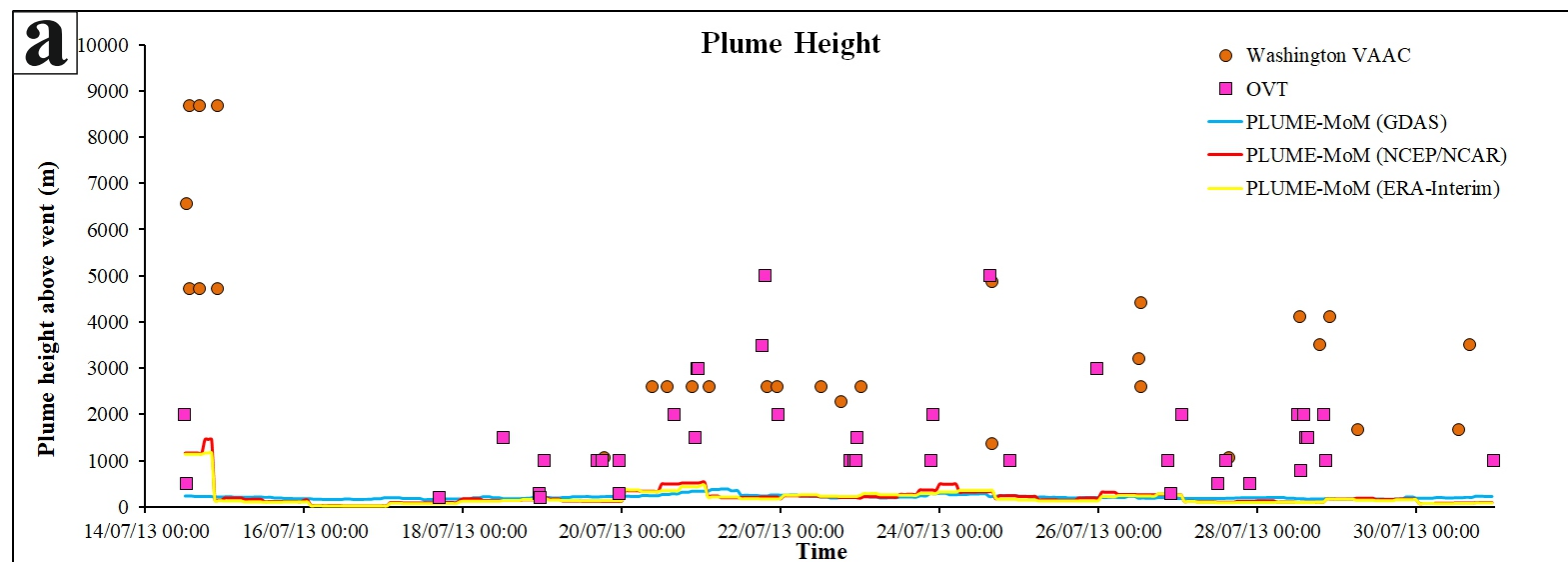


Figure 3.



**Figure 4.**



**Figure 5.**

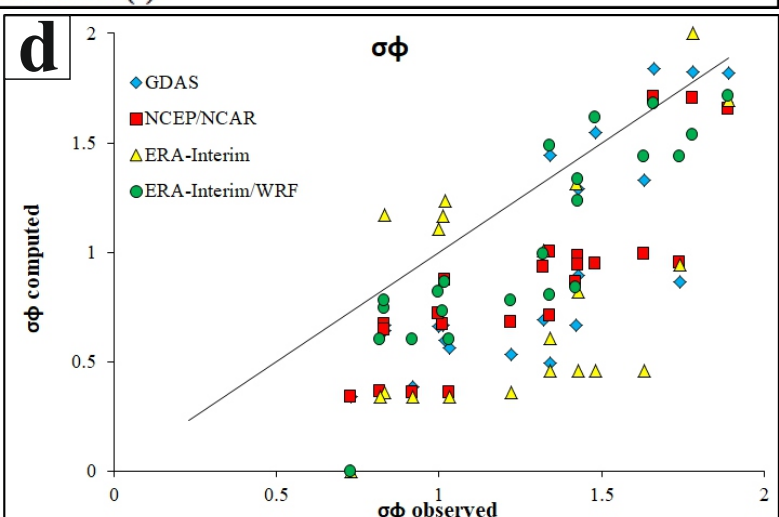
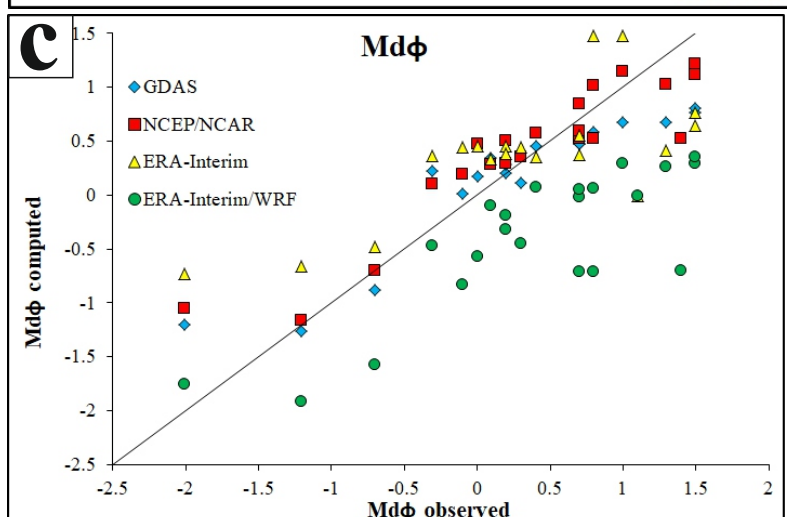
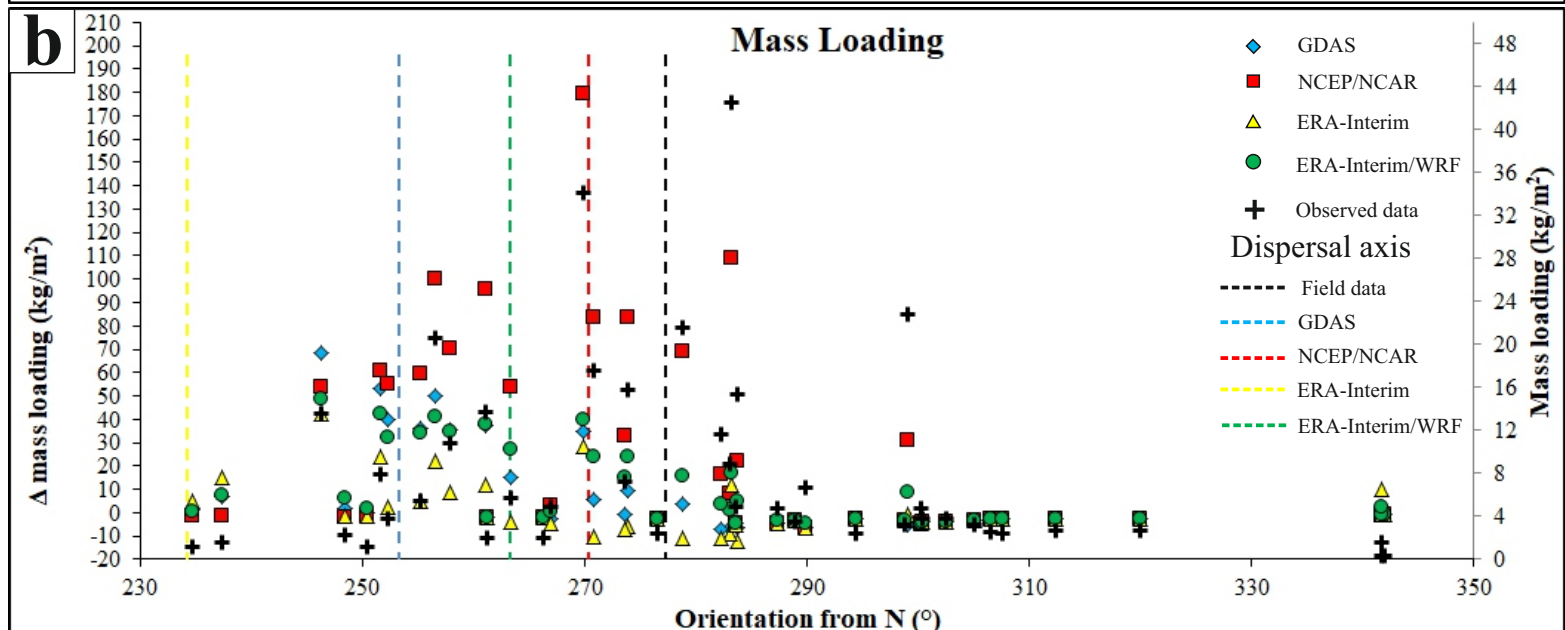
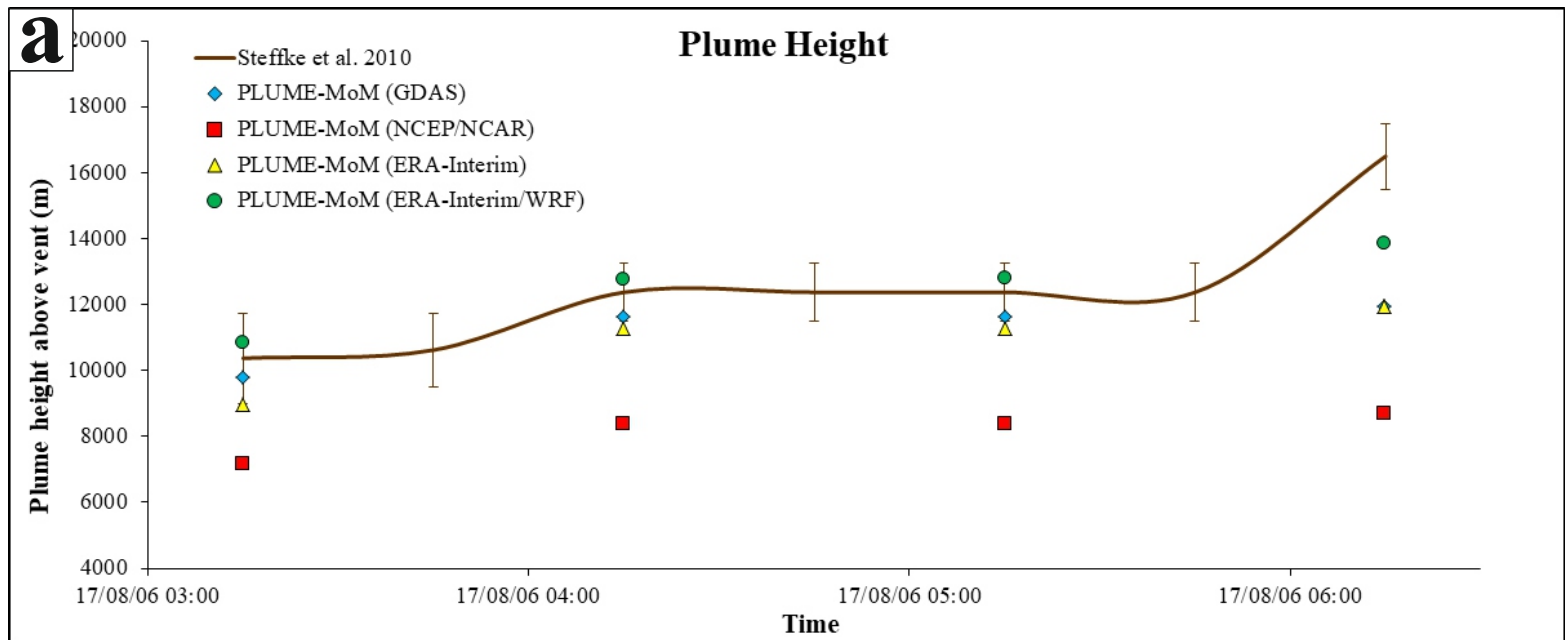


Figure 6.

